



Published in final edited form as:

Cell Rep. 2026 January 27; 45(1): 116729. doi:10.1016/j.celrep.2025.116729.

The RNA exosome maintains cellular RNA homeostasis by controlling transcript abundance in the brain

Lauryn A. Higginson¹, Xingjun Wang¹, Kevin He², Maggie Torstrick¹, Minho Kim³, H.R. Sagara Wijeratne⁴, Avery M. Runnebohm⁴, B  r  nice A. Benayoun^{3,5}, Adam MacLean⁶, Guillaume F. Chanfreau², Derrick J. Morton^{1,3,7,*}

¹ Molecular and Computational Biology, Department of Biological Sciences, University of Southern California, Los Angeles, CA 90089, USA

² Department of Chemistry and Biochemistry and the Molecular Biology Institute, University of California, Los Angeles, Los Angeles, CA 90095, USA

³ Leonard David School of Gerontology, University of Southern California, Los Angeles, CA 90089, USA

⁴ Indiana University School of Medicine, Department of Biochemistry and Molecular Biology, Center for Computational Biology and Bioinformatics, Indianapolis, IN 46202, USA

⁵ Department of Cancer Biology, University of Southern California Keck School of Medicine, Los Angeles, CA 90089, USA

⁶ Department of Quantitative and Computational Biology, University of Southern California, Los Angeles, CA 90089, USA

⁷ Lead contact

SUMMARY

Intracellular ribonucleases (RNases) are essential for maintaining accurate RNA levels. Inherited mutations in genes encoding ubiquitous RNases are associated with human diseases, primarily affecting the nervous system. Recessive mutations in genes encoding the evolutionarily conserved RNA exosome, an RNase complex, cause syndromic neurodevelopmental disorders, such as pontocerebellar hypoplasia type 1b (PCH1b), characterized by progressive neurodegeneration. Here, we establish a CRISPR-Cas9-engineered *Drosophila* model of PCH1b to investigate the cell-type-specific post-transcriptional regulatory functions of the RNA exosome complex *in vivo*. Pathogenic variants in Rrp40, a subunit of the complex, disrupt RNA exosome activity, leading to widespread transcriptomic dysregulation in brain-enriched cell populations, including defective rRNA processing. These molecular defects coincide with progressive neurodegeneration and

This is an open access article under the CC BY-NC license (<http://creativecommons.org/licenses/by-nc/4.0/>).

*Correspondence: mortond@usc.edu.

AUTHOR CONTRIBUTIONS

Conceptualization, L.A.H. and D.J.M.; methodology, L.A.H., A.M., and D.J.M.; investigation, L.A.H., X.W., M.T., K.H., M.K., H.R.S.W., and A.M.R.; writing – original draft, L.A.H. and D.J.M.; writing – review & editing, L.A.H., D.J.M., B.A.B., and G.F.C.; funding acquisition, L.A.H., B.A.B., H.R.S.W., A.M.R., and D.J.M.; resources, D.J.M., B.A.B., and G.F.C.; supervision, D.J.M.

DECLARATION OF INTERESTS

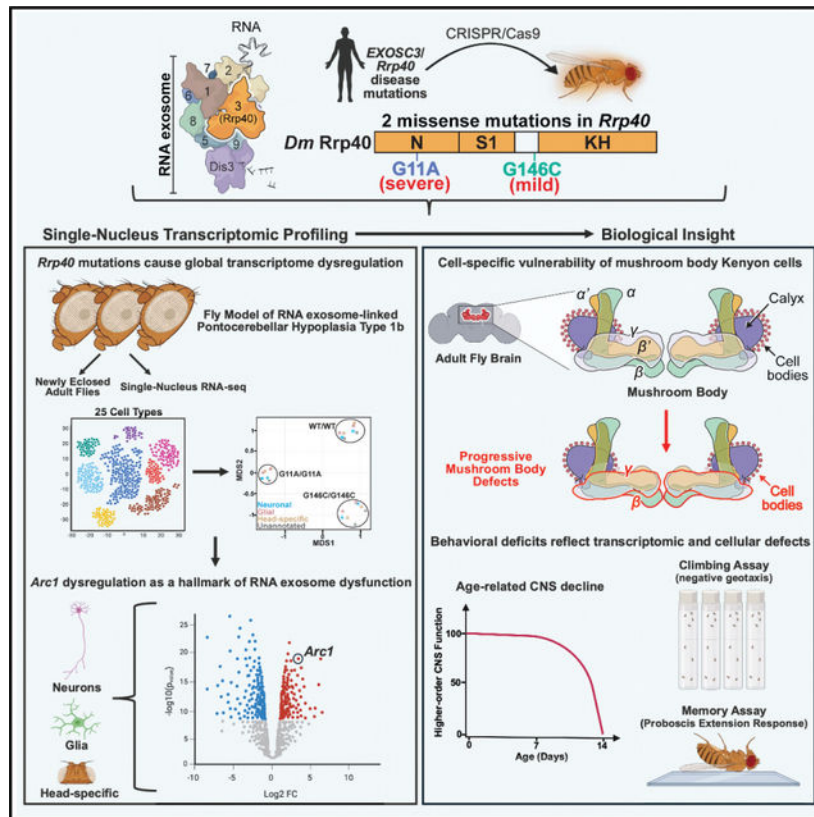
The authors declare no competing interests.

behavioral impairments that track with allele severity. Our findings provide a cell-type-resolved view of RNA exosome function in a fully developed animal brain and underscore the critical role of RNA surveillance in safeguarding transcriptome homeostasis and neuronal integrity.

In brief

Higginson et al. present a cell-type-resolved atlas of RNA exosome dysfunction in the *Drosophila* brain, showing that pathogenic *Rrp40* mutations disrupt RNA surveillance and neuronal integrity. This resource reveals how impaired RNA decay deregulates cell-type-specific transcriptomes and contributes to neurodegenerative mechanisms underlying pontocerebellar hypoplasia type 1b.

Graphical Abstract



INTRODUCTION

Intracellular transcriptome homeostasis relies on the strict regulation of RNA degradation and processing by ribonucleases (RNases), which safeguard cell function and integrity.^{1–3} RNases regulate gene expression co- and post-transcriptionally to balance cellular RNA levels,^{4–6} and their disruption causes pathogenic accumulation of coding RNA and non-coding RNA (ncRNA), leading to neurological disease.^{7–9} Variants in endonucleases and 3′-5′ endo/exoribonucleases cause disorders such as Aicardi-Goutières syndrome (AGS)^{10–12} and subtypes of pontocerebellar hypoplasia (PCH),^{13–18} whereas 5′-3′ exoribonucleases have not yet been directly implicated in neuropathology. These findings suggest that

the nervous system is uniquely vulnerable to RNase dysfunction, but the mechanisms underlying this hypersensitivity remain unclear.

Recessive missense mutations in genes encoding structural subunits of a 3'-5' RNase complex, the RNA exosome, cause syndromic neurodevelopmental disorders, most notably distinct PCH subtypes.^{17–20} The RNA exosome is a conserved 10-subunit complex with structural cap and core proteins that guide substrates to catalytic subunits Dis3 or EXOSC10/Rrp6 (illustrated in Figure 1A).^{21–25} The RNA exosome degrades all major classes of RNA^{26–29} with specificity enhanced by cofactors.^{30–34} While yeast models have provided structural insights into RNA exosome disease-associated amino acid changes,^{35–38} they do not capture how pathogenic mutations perturb the function of the complex in a multicellular organism. Animal studies have begun to fill this gap, including our prior *Drosophila* model of PCH type 1b (PCH1b), a subtype of PCH, which revealed a neuronal requirement for EXOSC3/Rrp40.³⁹ In addition, zebrafish loss-of-function studies have confirmed that RNA exosome activity is essential for brain development.^{18,37} Yet, despite these studies, it remains unresolved how pathogenic *EXOSC3/Rrp40* mutations disrupt cell-type-specific gene expression programs *in vivo* and lead to neuronal pathology.

To investigate the cell-type-specific consequences of neuropathy-causing RNA exosome mutations *in vivo*, we generated CRISPR-Cas9-engineered *Drosophila* models of PCH1b-linked variants in the EXOSC3 ortholog Rrp40 (severe: G11A/G11A; mild: G146C/G146C). Using single-nucleus RNA sequencing (snRNA-seq), long-read Nanopore profiling, confocal imaging, and behavioral assays, we show that *Rrp40* mutations disrupt RNA processing and cause widespread dysregulation of cellular transcriptomes in the fly brain.

Transcriptomic profiling revealed distinct allele- and cell-type-specific signatures, with *Arc1* emerging as a globally dysregulated transcript across neuronal and glial populations. *Arc1*, a regulator of synapse maturation and plasticity,⁴⁰ exemplifies how impaired RNA exosome surveillance alters neuronal RNA abundance in the brain. These molecular defects, including impaired rRNA processing, arise from compromised RNA exosome activity and coincide with progressive mushroom-body degeneration, reduced lifespan, and short-term memory impairments that track with allele severity, highlighting how distinct pathogenic variants differentially disrupt brain homeostasis. Importantly, pan-neuronal *Arc1* overexpression in aged flies disrupted mushroom-body morphology, underscoring the requirement for precise *Arc1* regulation. Together, our findings establish the RNA exosome as a central safeguard of cellular transcriptome homeostasis in the brain and provide mechanistic insight into the pathogenesis of PCH1b.

RESULTS

snRNA-seq of brain-enriched tissue from *Rrp40* mutant flies reveals distinct cell-type-specific gene expression signatures

To investigate RNA exosome function within the brain *in vivo*, we generated flies modeling PCH1b-causing mutations at the *Rrp40* locus via CRISPR-Cas9 technology. The RNA exosome is an evolutionarily conserved, multi-subunit complex (Figure 1A). EXOSC3/Rrp40 contains an N-terminal domain, an S1 RNA-binding domain, and a K-homology

(KH) RNA-binding domain (Figure 1B). Recessive missense mutations in *EXOSC3* (fly *Rrp40*) encoding single amino acid substitutions cause PCH1b with varying severity.^{18,41,42} Given that *EXOSC3* mutations cause tissue-specific neurodevelopmental defects leading to neurodegeneration in humans,¹⁸ we engineered *Drosophila* models of PCH1b to assess the functional consequences of these substitutions. Flies modeling wild-type (WT; Rrp40-WT) or mutant (Rrp40-G11A or Rrp40-G146C) alleles were validated by Sanger sequencing (Figure S1A). Homozygous mutants showed reduced viability compared to WT controls (WT/WT: 91%, $n = 91$; G11A/G11A: 19%, $n = 85$; G146C/G146C: 40%, $n = 70$; Figure 1D), consistent with prior results.³⁹ Western blotting confirmed reduced steady-state Rrp40 protein in both mutants (Figures S1B and S1C), validating that pathogenic alleles destabilize Rrp40 protein³⁹ and establishing the basis for subsequent analyses.

To assess cell-type-specific effects, we profiled nuclei from brain-enriched tissue of newly eclosed (day 1) WT/WT, G11A/G11A, and G146C/G146C flies using droplet-based snRNA-seq (Figure 1E). Two biological replicates (~20 heads per genotype) yielded 116,619 high-quality nuclei (Figures 1F, S1D, and S1E). Uniform manifold approximation and projection (UMAP) analysis showed distinct separation of G11A/G11A clusters, partial overlap of G146C/G146C with WT/WT, and minimal overlap between mutant genotypes, indicating allele-specific disruption of RNA exosome function (Figure 1F). We next integrated datasets (116,619 nuclei total; Figures 1F and S1F) and subdivided nuclei into broad classes (neuron, glia, and head specific) (Figure 1G). Using published marker genes,^{43–46} we manually annotated 25 cell types: eleven neuronal subtypes, seven glial subtypes, and seven head-specific populations (Figure 1H). As in prior fly brain datasets, ~43% of nuclei remained unannotated.^{43,45,46} UMAP projections of annotated cell types revealed distinct transcriptomic profiles across genotypes (Figures 1I and S2). Together, these data establish a high-quality snRNA-seq resource to interrogate whether RNA exosome function is broadly conserved across brain cell types or entails specialized requirements in specific cell populations.

Broad transcriptomic dysregulation occurs within brain-enriched tissue in *Rrp40* mutants

We leveraged our snRNA-seq dataset to evaluate how RNA exosome mutations impact cell-type-specific transcriptomes in brain-enriched tissue from *Rrp40* mutants (severe: G11A/G11A or mild: G146C/G146C) and control (WT/WT) flies. Multidimensional scaling (MDS) revealed clear genotype-dependent segregation among major brain cell classes (neuron, glial, head-specific, and unannotated), with samples clustering together within each genotype, indicating reproducible and global transcriptome differences (Figures 2A and S1F).

Differential expression analysis confirmed broader dysregulation in severe G11A/G11A mutants than mild G146C/G146C mutants (2,537 vs. 1,743 transcripts > 2-fold; Figure 2B), with the majority of altered RNAs increased, consistent with impaired RNA decay. Subpopulation-level analysis (> 100 cells per genotype) revealed strong allele-dependent transcriptomic signatures (Figures S3 and S4). UpSet analysis of neuronal and glial datasets revealed 60 shared transcripts and 512 (G11A/G11A) and 228 (G146C/G146C) allele-specific sets (Figure 2C). Gene Ontology (GO) enrichment analysis of the shared set

highlighted DNA repair, RNA-mediated transposition, and neuronal development (Figure 2D), supporting a role for the RNA exosome in processes spanning genome stability and neuronal signaling.

Analysis of allele-specific transcript sets revealed striking divergence in biological pathways and disease associations. G11A/G11A-specific transcripts were enriched for neurological pathways, including Alzheimer's orthologs *Gss1*, *Cyp9b2*, and *Pepck2*, whereas G146C/G146C-specific transcripts were linked mainly to metabolic disorders (Figure S5A). GO terms further distinguished alleles: G11A/G11A transcripts were enriched for DNA repair, stem cell division, and neuromuscular processes, while G146C/G146C transcripts were enriched for immune-related categories (Figure S5B). Together, these findings reveal that distinct PCH1b variants differentially affect RNA exosome activity across cell populations, with the severe allele causing broader disruption in both neuronal and glial subtypes. This allele- and cell-type specificity suggests that brain-enriched cell populations vary in their dependence on RNA surveillance, potentially reflecting differences in transcriptional load, metabolic activity, or ncRNA processing.

Arc1, a synaptic regulator, emerged as one of the most consistently increased transcripts. *Arc1*-positive cells increased from ~6% in controls to ~83% in G11A/G11A and ~40% in G146C/G146C (Figures 2E–2G). DotPlot analysis demonstrated global *Arc1* dysregulation across nearly all cell types in G11A/G11A, with more restricted, Kenyon cell-enriched expression in G146C/G146C (Figure S5C). Validation confirmed persistent *Arc1* dysregulation: hybridization chain reaction (HCR) RNA fluorescence *in situ* hybridization (RNA-FISH) showed increased abundance and abnormal distribution persisting with age (Figures 2H, 2I, S5D, and S5E), with both aged *Rrp40* mutant alleles exhibiting comparably elevated *Arc1* levels and no significant difference between G11A/G11A and G146C/G146C, and proteomics confirmed increased *Arc1* protein levels in G11A/G11A heads (Figure S5F). To test whether *Arc1* loss affects neuronal morphology, we depleted *Arc1* in mushroom bodies (*R13-Gal4>Arc1^{IR}*) and observed no defects by FasII staining in aged flies (Figure S5G). Because FasII does not reliably stain γ -lobes, we additionally used disc-large (DLG) immunostaining to assess γ -lobe morphology. DLG staining of aged *Arc1^{esm113}* loss-of-function flies (BDSC #37531) showed normal γ -lobe morphology (Figures S5H and S5I), indicating that *Arc1* loss does not alter mushroom-body architecture. Together, these data establish *Arc1* as a highly sensitive transcript whose regulation depends critically on intact RNA exosome activity.

Because global analyses indicated widespread transcriptomic dysregulation, we next examined whether specific neuronal populations were disproportionately affected. Subclustering of Kenyon cells uncovered distinct genotype-specific transcriptome signatures (Figure S6A), with the majority of altered RNAs increased in G11A/G11A (57% vs. 49% in G146C/G146C; Figure S6B). GO enrichment highlighted ncRNA processing, DNA repair, and rRNA processing among increased transcripts, while decreased transcripts included axon development and synaptic pathways (Figures S6C and S6D). These findings suggest that brain-enriched cell types differ in their vulnerability to *Rrp40* variants, likely due to differences in their transcriptional and metabolic activity.

Neurotransmitter profiling further linked Rrp40 variants to alterations in neuronal signaling. Vesicular acetylcholine transporter (VACHT) expression was elevated in G11A/G11A (~33% of head cells; 0.59 in Kenyon cells) and G146C/G146C (~20%; 0.55) compared to controls (~21%; 0.36), whereas vesicular glutamate transporter (VGlut) and glutamate decarboxylase 1 (Gad1) remained unchanged (Figure S6E–S6H). Given the mushroom body's role in learning and memory,⁴⁷ these results suggest that cholinergic signaling imbalances, combined with reduced Kenyon cell numbers (Figure 4) and synaptic pathway disruption (Figures S6C and S6D), converge to compromise higher-order CNS function. Thus, while *Arc1* dysregulation occurs broadly, Kenyon cells represent a particularly sensitive population where allele-specific transcriptomic defects intersect with disrupted cholinergic signaling, providing a mechanistic link between global RNA exosome dysfunction and selective neuronal vulnerability.

Rrp40 mutants impair pre-rRNA processing in brain-enriched tissue

The RNA exosome was first identified for its essential role in pre-rRNA processing and is required for *in vivo* 3' end maturation of 5.8S rRNA.^{22,48} To evaluate whether pathogenic RNA exosome mutations alter rRNA biogenesis in *Drosophila* (Figure 3A), as shown in yeast modeling RNA exosome-linked PCH1b mutations,³⁶ we analyzed pre-rRNA processing in flies modeling PCH1b variants. Using near-infrared northern (irNorthern) blotting⁴⁹ on RNA isolated from brain-enriched tissue of newly eclosed (day 1) flies, we observed that *Rrp40* mutants accumulated intermediate precursor rRNAs and apparent 3' extended forms of 5.8S rRNA compared to control flies (Figure 3B). These defects were more pronounced in severe *Rrp40* mutants (G11A/G11A) relative to mild mutants (G146C/G146C).

To precisely assess how pathogenic RNA exosome mutations impact rRNA biogenesis in brain-enriched tissue, we applied long-read Nanopore-based RNA-seq to *in vitro* polyadenylated total RNA from 3 independent pooled replicates of newly eclosed (day 1) *Rrp40* mutant and control fly heads, as described in the STAR Methods. We used low-density Flongle sequencing cells because the abundance of rRNAs enabled us to utilize low-density cells and obtain sufficient information on rRNA accumulation. From our Nanopore RNA-seq data, we generated northern-blot-like images from an R-based package named Nanoblot, which includes the generation of nanoprobe that can be used to target specific RNAs.⁵² Nanoblot analysis using a 5.8S probe recapitulated the irNorthern blot results (Figure 3C), and Integrative Genome Viewer (IGV) mapping revealed increased 5.8S species extending into ITS2 (highlighted with a blue * in Figure 3D) and impaired degradation of 2S-ITS2 products in mutants (highlighted with a red * in Figure 3D). Quantification confirmed that severe *Rrp40* mutants had an elevated ratio of 5.8S extensions (~0.2 when normalized to mature 5.8S rRNA) compared to mild mutants and controls (~0.1) (Figure 3E). The Nanoblot in Figure 3F further revealed an ~400-nt 2S-ITS2 extension in *Rrp40* mutants compared to control flies. Consistent with the role of the RNA exosome in 3' end maturation, *Rrp40* mutants accumulated aberrant rRNAs, including ~450-nt extended 5.8S precursor species (abundance was normalized to mature 5.8S), whose identity was independently confirmed by Nanopore sequencing. These findings demonstrate that pathogenic mutations disrupt RNA-exosome-dependent rRNA maturation.

***Rrp40* mutant flies exhibit age-dependent mushroom-body γ - and β -lobe defects**

To investigate the impact of *Rrp40*-linked transcriptomic dysregulation (Figures 2B, 3A–3F, S3, and S4) on neuronal homeostasis within the fly brain, we assessed the neuroarchitecture of the fly central complex (Figure 4A) and the mushroom body (Figure 4B). The central complex, responsible for higher-order sensory and motor functions,⁵³ consists of the fan-shaped body (FB), protocerebral bridge (PB), ellipsoid body (EB), and antennae lobes (ALs). The mushroom body, the seat of learning and memory in *Drosophila*, is composed of ~2,000 intrinsic Kenyon cells, whose dendrites form the calyx, and axons project through the peduncle to form the mushroom-body lobes (α -, β -, α' -, β' -, and γ -lobes).^{54,55}

We analyzed the central complex in *Rrp40* mutants (G11A/G11A or G146C/G146C) and control flies (WT/WT) by immunostaining for DLG, a post-synaptic neuronal marker, on day 1 and 14 brains. Confocal imaging revealed no morphological abnormalities in control flies (WT/WT, $n = 10$) or mild mutants (G146C/G146C, $n = 10$) at day 1, while severe mutants (G11A/G11A, $n = 10$) exhibited a mild reduction in FB size (Figure 4C). By day 14, both severe (G11A/G11A, $n = 10$) and mild (G146C/G146C, $n = 10$) mutants displayed reduced AL and FB sizes, without gross structural defects (Figure 4D). We conclude that central complex morphology is largely preserved, though reduced in size, in *Rrp40* mutants.

Building on the *Rrp40*-linked transcriptomic dysregulation we observed in mushroom-body Kenyon cell types (Figure S6), we next examined mushroom-body architecture using flies expressing GFP under the mushroom-body-specific driver *R13F02-Gal4*, co-stained with DLG. On day 1, G11A/G11A mutants ($n = 10$) showed β -lobe midline crossing and thinning γ -lobes compared to controls, while G146C/G146C mutants ($n = 10$) showed no overt abnormalities. By day 14, both mutants exhibited progressive γ -thinning, with persistent β -lobe midline crossing in G11A/G11A mutants (Figure 4E). Quantification confirmed significant reductions in γ -lobe size and β -lobe midline distance in aged mutants (Figures 4F–4I). Importantly, targeted expression of *EXOSC3* (*UAS-EXOSC3-myc*) in mushroom bodies (*R13F02-Gal4*) rescued both phenotypes in G11A/G11A flies, demonstrating functional conservation of *EXOSC3* and *Rrp40* (Figures 4J–4L). Additional validation with FasII immunostaining showed progressive α -, β -, and γ -lobe thinning in aged mutants, with severe G11A/G11A flies displaying near-complete loss of γ -lobes (Figure S7A). Similarly, RNAi-mediated depletion of *Rrp40* in mushroom bodies caused progressive γ -lobe degeneration (Figures S7B–S7D), reinforcing that *Rrp40* is essential for mushroom-body neuronal homeostasis.

Together, these results demonstrate that *Rrp40* is required for proper mushroom-body morphogenesis and homeostasis, while the central complex architecture remains grossly intact.

***Rrp40* mutant fly brains exhibit decreased neuronal cell populations and mushroom-body Kenyon cell death**

Given that we observed progressive mushroom-body defects in *Rrp40* mutant flies (Figures 4E and S7A–S7D), we next asked whether these structural abnormalities reflect underlying changes in cellular composition. To address this, we leveraged our snRNA-seq dataset

and applied a cell proportion analysis tool designed for single-cell (sc)/snRNA-seq.⁵⁶ This allowed us to quantify the relative abundance of neuronal, glial, and head-specific cell populations in day 1 *Rrp40* mutant and control flies. We found that *Rrp40* mutants exhibited a significant reduction in neuronal populations ($>1.25 \log_2$ fold difference [$\log_2\text{FD}$], false discovery rate [FDR] < 0.05), whereas severe G11A/G11A mutants showed no changes in glial, head-specific, or unannotated cell classes (Figure 5A). In contrast, mild G146C/G146C mutants displayed a significant increase in head-specific cells without alterations in glial or unannotated populations. To further dissect these effects, we expanded our analysis across all 25 annotated brain cell types (Figure S7E), revealing an inverse relationship in medullary intrinsic neurons (Mis) and transmedullary neurons (Tm1s): increased in G11A/G11A mutants but reduced in G146C/G146C compared to WT/WT. These results suggest that RNA exosome dysfunction destabilizes neuronal homeostasis and alters specific cellular proportions in a genotype-dependent manner.

In parallel, we observed an increased proportion of unannotated cells in both *Rrp40* mutants compared to controls and published datasets,^{43,45} particularly in G11A/G11A flies, which contained ~3,000 more unannotated cells than controls. This finding raises the possibility that transcriptome-wide dysregulation obscures molecular identities in snRNA-seq, leading to apparent neuronal loss that may reflect annotation failure rather than the absence of cells. Such masking effects appear especially pronounced in the severe allele and underscore how RNA exosome dysfunction may compromise cell identity at the transcriptional level.

Because Kenyon cells are central to mushroom-body function and particularly sensitive to *Rrp40* loss (Figure 4E), we next examined mushroom-body Kenyon cell subpopulations in detail. Cell proportion analysis revealed significantly fewer α , β , α' , β' , and γ Kenyon neurons in both mutants compared to controls ($>1.25\log_2\text{FD}$, FDR < 0.05), with a concurrent increase in unannotated Kenyon cells (Figure 5B). To directly test whether these apparent reductions reflected cell death, we performed immunostaining for the apoptotic effector caspase Dcp1 in control and *Rrp40* mutant brains. Kenyon cell bodies are tightly packed around the calyx (Kenyon cell dendrites) (Figure 5C), with each Kenyon cell body dendrite occupying a small proportion of the calyx. Thus, utilizing engineered *Rrp40* control and mutant flies expressing a Gal4-specific driver for mushroom bodies combined with a *UAS-GFP* transgene (*Rrp40/Rrp40; R13F02>Gal4/UAS-GFP*), we immunostained whole adult fly brains for Kenyon cell bodies/calyx (green), Dcp1 (magenta), and DAPI (blue). We imaged from both the posterior and posterior-medial views to gain a comprehensive understanding of Kenyon cell body cell death, given that Kenyon cell bodies wrap around the calyx (Figure 5C). On day 1, both G11A/G11A and G146C/G146C mutants already displayed elevated percentages of Dcp1+ Kenyon cell bodies compared to controls (Figures 5D and 5E). By day 14, G146C/G146C mutants retained similar levels of apoptosis, whereas G11A/G11A mutants showed a significant accumulation of Dcp1+ cells relative to both controls and G146C/G146C. Consistent with this, G11A/G11A mutants also exhibited reduced Kenyon cell body numbers and decreased calyx area, while G146C/G146C mutants did not show significant structural changes despite a modest rise in apoptosis (Figures 5E–5G).

Taken together, these results demonstrate that the severity of RNA exosome dysfunction in *Rrp40* mutants determines the extent of neuronal vulnerability. While both alleles impair mushroom-body homeostasis, the severe G11A/G11A mutation leads to progressive Kenyon cell death, loss of neuronal architecture, and disruption of calyx structure. We conclude that *Rrp40* activity is essential for maintaining mushroom-body morphogenesis and neuronal homeostasis in the adult fly brain.

***Rrp40* mutants exhibit age-dependent locomotor and taste learning and memory deficits**

The central complex and mushroom body are key regions of the fly brain linked to advanced neuronal functions, including locomotion, learning, and memory.^{57–59} Based on cellular and transcriptomic changes observed in *Rrp40* mutants, we tested whether these defects translated into measurable organismal phenotypes. Kaplan-Meier analysis revealed significantly shortened lifespans in *Rrp40* mutants compared to controls (WT/WT). Severe G11A/G11A mutants died by day 22, whereas mild G146C/G146C mutants survived until ~day 40, both significantly reduced relative to controls, which survived beyond 70 days (Figure 6A).

To evaluate CNS functionality, we conducted negative geotaxis assays on *Rrp40* mutants and controls. Both mutants displayed progressive locomotor decline with age, with severe G11A/G11A flies failing to climb by day 14 (Figure 6B), consistent with prior findings.³⁹ Importantly, pan-neuronal expression of human *EXOSC3* under the *nSyb*-Gal4 driver significantly increased locomotor performance in G11A/G11A mutants (*G11A/G11A;nSyb-Gal4/UAS-EXOSC3*), restoring climbing ability toward control levels (Figure 6C).

Finally, to test whether associative memory formation in the mushroom body is compromised in *Rrp40* mutants, we conducted short-term aversive taste assays as described in the STAR Methods. Aged G11A/G11A displayed marked memory deficits, with 50% of flies responding to the tastant (sucrose) on day 14, while G146C/G146C and WT/WT controls performed normally (Figure 6D). Pan-neuronal *EXOSC3* expression rescued memory performance in G11A/G11A flies (Figure 6E). Together, these results demonstrate that *Rrp40* mutations disrupt both locomotor and cognitive function through CNS impairment, and the restoration of RNA exosome activity can restore these phenotypes.

***Arc1* overexpression contributes to age-dependent mushroom body defects**

To directly test whether specific dysregulated transcripts contribute to neuronal phenotypes in *Rrp40* mutants, we focused on *Arc1*, which shows disproportionately increased mRNA levels in mutants (Figures 2E–2I). Using the Gal4/UAS system, we overexpressed *Arc1* either in a pan-neuronal or Kenyon cell-specific manner. We first validated steady-state *Arc1* protein levels: head immunoblots from control flies (*w¹¹¹⁸*, *elav*>Gal4, or *UAS-Arc1*) and flies expressing *Arc1* under the pan-neuronal driver (*elav*>Gal4)⁶⁰ confirmed elevated multimeric and monomeric *Arc1* species (Figure 7A), detected with a validated *Arc1* antibody.⁴⁰ *Arc1* monomers are known to form retrovirus-like capsids that package *Arc* mRNA for transsynaptic transfer,^{40,61} and such transfer is required for synaptic plasticity in *Drosophila*.⁴⁰

Rrp40 mutants exhibit mushroom-body defects (Figures 4E–4I and S7A) and elevated *Arc1* mRNA levels in mushroom-body neurons compared to WT controls (Figures S5C and S6). To test whether *Arc1* overexpression alone is sufficient to cause similar defects, we analyzed the brains of flies expressing *Arc1* in Kenyon cells with *F13F02*-Gal4 and *UAS*-GFP. On day 1, *Arc1*-overexpressing flies showed no overt mushroom-body abnormalities compared to controls (Figures 7B and 7C). By day 21, however, *Arc1* overexpression produced γ -lobe thinning (Figures 7D and 7E). These findings demonstrate that precise *Arc1* regulation is necessary for mushroom-body morphology, but *Arc1* overexpression alone does not fully recapitulate the *Rrp40* mutant phenotype. Taken together with the behavioral impairments described above, these data highlight *Arc1* dysregulation as an outcome of RNA exosome dysfunction that contributes to age-dependent structural and functional brain defects.

DISCUSSION

This study provides the first cell-type-resolved transcriptome analysis of mutants defective for an RNase complex across distinct cell populations within a fully developed animal brain. Specifically, we investigate the effects of the RNA exosome complex on cell-type-specific RNA levels within brain-enriched tissue in *Drosophila* by studying neuropathy-causing RNA exosome variants. By modeling pathogenic RNA exosome variants of the EXOSC3 ortholog Rrp40 that cause PCH1b,¹⁸ we demonstrate that RNA exosome dysfunction leads to widespread dysregulation of RNA abundance across diverse cell types. Using droplet-based snRNA-seq, we found that both severe (G11A/G11A) and mild (G146C/G146C) mutants exhibit broad transcriptomic changes, including the accumulation of functionally important neuronal transcripts such as *Arc1*. Nanopore sequencing further revealed defects in rRNA biogenesis, confirming that pathogenic alleles disrupt canonical RNA exosome functions. These molecular alterations were accompanied by progressive mushroom-body defects, reduced locomotor ability, and impaired learning and memory phenotypes that parallel neurodegenerative outcomes in flies⁶² and align with PCH1b clinical severity. Finally, we show that pan-neuronal overexpression of *Arc1* disrupts mushroom-body morphology, underscoring the importance of precise *Arc1* regulation for neuronal integrity.

Our findings highlight a paradox: although the RNA exosome is a ubiquitously expressed RNase complex essential for RNA metabolism,^{1,29,63} mutations in structural subunit genes of the RNA exosome cause tissue-specific neuropathology.⁹ By comparing two PCH1b-linked alleles, we observed that the severe G11A/G11A variant induces greater transcriptome dysregulation than the mild G146C/G146C allele, consistent with genotype-phenotype correlations in patients¹⁹ and our previous work in flies.³⁹ This supports the view that distinct mutations differentially compromise RNA exosome activity. Notably, dysregulation was not confined to neurons but spanned all cell populations, revealing the broad role of the RNA exosome in maintaining transcriptome homeostasis *in vivo*.

Consistent with the role of the RNA exosome in RNA decay,^{29,64} most affected transcripts were increased, likely reflecting impaired degradation of direct RNA targets. Among these, *Arc1* emerged as the most consistently elevated across neurons and glia, with both transcriptomic and proteomic analyses confirming *Arc1* accumulation. Given the role of *Arc1* in synaptic plasticity, *Arc1* dysregulation may contribute to the neuronal

vulnerability observed in *Rrp40* mutants. Similarly, we observed elevated VACHT transcript levels, suggesting potential cholinergic signaling defects. While unvalidated at the protein level, these changes mirror phenotypes of cholinergic dysfunction in flies^{65–67} and align with human neurological disorders involving cholinergic impairment.^{68–70} These findings highlight cholinergic dysregulation as an intriguing avenue for future investigation into how RNA exosome dysfunction perturbs neurotransmission.

Beyond global transcriptomic disruption, our single-nucleus analyses uncovered allele- and cell-type-specific differences that likely reflect variable requirements for the RNA exosome across diverse brain cell populations. The severe G11A/G11A allele produced widespread dysregulation across both neuronal and glial populations, whereas the milder G146C/G146C mutations resulted in more restricted, subtype-specific effects. These findings suggest that individual cell types vary in their reliance on RNA surveillance, potentially due to differences in transcriptional burdens, metabolic activity, or the processing and maturation of ncRNAs.^{71,72} Notably, neuronal classes enriched for activity-regulated transcripts, such as *Arc1*, or those heavily engaged in synaptic signaling appear particularly vulnerable to impaired RNA decay. This selective sensitivity may explain why certain neuronal populations, such as mushroom-body Kenyon cells, display greater susceptibility to RNA exosome dysfunction. Importantly, our cell-type-resolved transcriptomic dataset provides a framework to dissect how specific RNA exosome mutations perturb both neuronal and glial subtypes with different functional and metabolic demands, offering a resource to probe tissue-specific RNA decay mechanisms *in vivo*. Future studies aimed at defining direct RNA exosome interactions with key signaling pathways, such as cholinergic transmission, will be essential for understanding how these cell-type-specific vulnerabilities give rise to neuropathology.

Together, our findings establish that RNA exosome dysfunction drives transcriptome-wide disruption across brain cell types, destabilizing both coding RNA and ncRNA pathways. Although neurons, particularly mushroom-body Kenyon cells, display heightened sensitivity, global dysregulation suggests a fundamental role for the RNA exosome in maintaining brain homeostasis. By linking molecular, cellular, and behavioral outcomes, this work provides mechanistic insight into how pathogenic RNA exosome mutations contribute to PCH1b and more broadly illustrates how impaired RNA surveillance can converge on neurodevelopmental and neurodegenerative pathologies.

Limitations of the study

Our study has several limitations. First, all experiments were performed in adult flies modeling RNA exosome-linked PCH1b; therefore, we cannot exclude the possibility that *Rrp40* functions earlier in development to influence neuronal homeostasis in adulthood. Second, while we define a role for *Rrp40* in maintaining cellular homeostasis within the fly brain, all experiments were conducted in adult female flies; thus, potential sex-specific differences in *Rrp40*-linked transcriptome regulation remain unresolved.

RESOURCE AVAILABILITY

Lead contact

Requests for further information and resources should be directed to and will be fulfilled by the lead contact, Derrick J. Morton (mortond@usc.edu).

Materials availability

All unique/stable reagents generated in this study are available from the lead contact with a completed materials transfer agreement.

Data and code availability

- snRNA-seq data have been deposited at NCBI GEO at accession number GEO: GSE280166 and are publicly available as of the date of publication.
- Nanopore-based data have been deposited at the NIH Sequence Read Archive (SRA) under BioProject: PRJNA1179429 and are publicly available as of the date of publication.
- All scripts used to analyze this dataset are available on the Morton lab GitHub at <https://github.com/themortonlab/flyprojects> and Zenodo (<https://doi.org/10.5281/zenodo.17555725>). These scripts are publicly available as of the date of publication.
- Raw and processed mass spectrometry data are available via ProteomeXchange partner MassIVE with accessions MSV000099840 and PXD070589 (doi:10.25345/C5J67992X) and are publicly available as of the date of publication.
- Any additional information required to reanalyze the data reported in this paper is available from the lead contact upon request.

STAR★METHODS

EXPERIMENTAL MODEL AND STUDY PARTICIPANT DETAILS

Fly husbandry: All crosses were maintained under standard conditions at 25°C using a standard agar/dextrose/corn meal/yeast media. Stocks used in this study include: *R13F02>Gal4*, *elav>Gal4* (BDSC #48571), *nSyb>Gal4* (BDSC #51635), *UAS-Arc1.WT* (BDSC #37532), *Arc1^{esm113}* (BDSC # 37531), *UAS-EXOSC3-myc* (generated at Bestgene, Inc. (CA)), *UAS-GFP* (BDSC #32195), and the RNA knockdown lines: Control TRiP RNAi (BDSC#36304), *UAS-Rrp40^{RNAi}* (TRiP HMJ23923, BDSC #62834), and *UAS-Arc1^{RNAi}* (TRiP JF01974, #25954) were obtained from the Bloomington *Drosophila* Stock Center (Indiana, US). *Rrp40^{G11A}* and *Rrp40^{G146C}* were generated by CRISPR/Cas9 editing at Bestgene, Inc. (CA).

METHOD DETAILS

Generation of CRISPR-Cas9 fly stocks: *Rrp40* mutants and wildtype controls were generated using CRISPR/Cas9-mediated gene editing as described previously.³⁹ *pU6-*

gRNAs: Target-specific sequences were identified using DRSC flyCRISPR optimal target finder (<https://www.flyrnai.org/crispr/>). HDR donor vectors (Emory Integrated Genomics Core) were constructed by cloning a 3kb fragment of the *Rrp40* locus into the *KpnI*/*SmaI* sites of the *pBlueScript-II* vector, with a loxP-flanked *3xP3-DsRed* cassette inserted downstream of the *Rrp40* 3' UTR. Point mutations corresponding to G11A and G146C were introduced into this backbone. The *3xP3-DsRed* cassette allows positive selection based on red fluorescence in the adult eye. Embryo injections (500 ng/μL HDR and 250 ng/μL U6-gRNA plasmid) were performed in *nos-Cas9* embryos by Besgene, Inc. Transformants were screened for dsRed fluorescence, and mutations were confirmed by Sanger Sequencing at the *Rrp40* locus. All CRISPR-edited lines were backcrossed (*w¹¹¹⁸*) for nine generations before use.

Single-nuclei RNA sequencing

Fly head preparation and nuclei dissociation: Two biological replicates of newly eclosed adult female flies were prepared for each biological replicate (*Rrp40^{WT}*, *Rrp40^{G11A}*, and *Rrp40^{G146C}*). For each sample, 20 fly heads were pooled together, and nuclei were isolated using the methods adopted from.^{79,80} Heads were homogenized on ice in 1000μL of homogenization buffer (nuclease-free water, sucrose, 10mM Tris (pH 8.0), 25 mM KCl, 5 mM MgCl₂, 0.1% Triton X-100, RNasin Plus, 1x protease inhibitor, and 0.1mM DTT) using a 1mL Dounce homogenizer. Homogenization was performed with 20 passes of the loose pestle followed by 40 passes of the tight pestle. The homogenate was filtered through a 70μm cell strainer into a 15mL conical pre-coated with 5% Bovine Serum Albumin (BSA). 4mL of nuclei wash buffer (0.5% BSA, PBS, and RNasin Plus) was added over the filter, and the samples were centrifuged; the supernatant was discarded. A second wash was performed with 5mL wash buffer, followed by centrifugation and removal of the supernatant. The pellet was re-suspended in 1mL wash buffer and transferred to a fluorescence-activated cell sorting (FACS) tube. Debris was removed by adding 600μL of debris removal solution (Miltenyi Biotec, Cat# 30-109-398) beneath 2mL resuspension buffer (0.5% BSA, PBS, RNasin) layered slowly on top. Samples were centrifuged, washed again in wash buffer using a wide-bore pipette tip. The nuclei suspension passed through a 40μm Flowmi strainer and assessed for quality and quantity by propidium iodide staining and flow cytometry. Only samples with < 30% debris content were used for library preparation.

10× Genomics single-nuclei library preparation: Single-cell libraries were prepared using Chromium Next GEM Single Cell 3' GEM, Library & Gel Bead Kit v3.1 (10X Genomics, PN-1000213) following the manufacturer's protocol (10x Genomics User Guide Chromium Next GEM Single-cell 30 Reagent Kits v3.1 (CG000204, Rev D)). Based on cell counts estimated from flow cytometry, nuclei suspensions were loaded to target a recovery of 10,000 nuclei per sample. Prepped libraries were quantified using a Qubit 3.0 Fluorometer (Thermo Fisher Scientific, Q33216) and quality assessed on a 4200 TapeStation system (Agilent Technologies; G2991A) with High Sensitivity D1000 DNA ScreenTape (Agilent Technologies 50675584). Sequencing was performed on an Illumina Novaseq 6000 platform generating 150 bp paired-end reads (Novogene USA).

Data processing and computational analysis: Reads were mapped to the *D. melanogaster* (r6.25) BDGP reference genome using Cell ranger version 7.1.0 (10X Genomics) with custom reference built as described in.⁸¹ Quality control was performed in R v4.1.1 using Seurat version v4.2.1,^{74–76} removing dead or low-quality cells and retaining those with 300–4000 UMIs and <10% mitochondrial reads. Post quality control, nuclei from all genotypes were merged and normalized with SCTransform v0.3.5. Dimensionality reduction was performed using PCA followed by 2D UMAP (30 dimensions, resolution 5) Cluster annotation was based on established cell-type markers,^{43,45} after which cells were categorized as neuronal, glial, head-specific, or unannotated. Pseudobulk analysis was conducted with Muscat v1.8.2 and DESeq2 v1.34.0. Subclustering of all major cell types, including Kenyon cells, using the Seurat subset function. Differential expression results were validated in Loupe Browser v8 (10x Genomics). An UpSet plot (R v4.1.1) was generated to compare transcripts elevated in neuronal and glial cells of *Rrp40* mutants (G11A/G11A and G146C/G146C) at log₂FC > 2. Gene ontology enrichment of overlapping transcripts was performed using the FlyEnrichr database.^{82–84}

Sample preparation for quantitative proteomics of Arc1 protein: Cell lysates were prepared from three biological replicates, each consisting of 100 heads from wild-type and mutant genotypes. Lysates were produced under liquid nitrogen grinding and then approximately 50ug of total lysate per biological sample was subjected to LysC/Trypsin digestion and tandem mass tag (TMT) labeling as previously described.⁸⁵ Labeled samples were combined into a multiplex and subjected to high pH basic reversed phase fractionation into a total of eight fractions for this analysis. Fractions were run by Nano-LC-MS/MS using an Orbitrap Eclipse mass spectrometer (Thermo Fisher Scientific) coupled to an EASY-nLC system (Thermo Fisher Scientific). Data was analyzed against a Drosophila FASTA database also containing common lab contaminants including proteolytic enzymes through Proteome Discoverer 2.5 using the search algorithm SEQUEST HT as previously described.⁸⁵

Hybridization chain reaction RNA-fluorescent *in situ* hybridization + IHC: This protocol was adapted from the Molecular Instruments HCR IF + HCR RNA-FISH protocol for samples in solution. Brain dissections and staining were performed as described previously.^{39,86} Brains from anesthetized flies were dissected in 1x PBS, transferred into PBS-tween (0.2%), and fixed overnight at 4°C in 4% paraformaldehyde (32% PFA, Electron Microscopy Sciences, Cat #15714-S). Fixed brains were washed in PBS-tween and preserved overnight at 4°C in 100% methanol. Tissues were rehydrated, permeabilized with 0.3% PBS-Triton for 20 min at room temperature, blocked in antibody diluent (Molecular Instruments) for 30 min, and incubated overnight at 4°C with primary antibody CadN (anti-Cadherin, DSHB; 1:50). Following washes, brain were incubated overnight at 4°C with the initiator-labeled secondary antibody (1:500), washed again, and post-fixed in 4% PFA for 10 min at room temperature. Samples were washed in 5x SSCT, pre-hybridized in probe hybridization buffer (Molecular Instruments) for 15 min at 45°C, then incubated overnight at 45°C with 0.2 pmol of 1µM DNA probes complementary to *Arc1* mRNA (designed by Molecular Instruments). After washing in Probe Wash Buffer and 5x SSCT, brains were blocked with amplification buffer for 15 min at room temperature. 2µL of each activated

(snap-cooled) fluorescently labeled hairpins were added to the amplification buffer, and samples were incubated overnight in the dark. Brains were washed in 5x SSCT, mounted in ProLong Gold Antifade Mountant, and imaged on a Zeiss LSM 880 confocal microscope at 20X magnification. Image processing and quantification were performed using Imaris software, with quantification based on the mean maximum fluorescence intensity per sample. Statistical analyses were conducted in PRISM (GraphPad, San Diego).

Near-infrared fluorescent northern blot: DNA probes were prepared by click-labeling azide modified DNA oligonucleotides with infrared dyes. Briefly 2.5 μ L of azide-modified DNA probe (100 μ M) was combined with 100 μ L of either IRDye 680RD (50 μ M) or IRDye 800CW (50 μ M) and brought to 1mL with PBS. Probes were incubated at 25°C for 6h to complete click-chemistry conjugation and purified with Ampure XP beads according to manufacturer's instructions. For blotting 5.5 μ g of total RNA was isolated from *Rrp40* controls (WT/WT) and mutants (G11A/G11A and G146C/G146C), mixed with 2X loading dye, and separated on a Mini-PROTEAN TBE-Urea gel (10% 10-well, 30 μ L) at 200V for 60 min. Gel migration was verified by ethidium bromide staining. RNA was transferred onto a Hybond N+ membranes and UV cross-linked with 254nm UV light (120mJ/cm² for 2 min) using a Stratalinker 2400. Membranes were prehybridized with pre-heated ExpressHyb solution for 30 min at 37°C, then hybridized at 37°C in the dark with 30 μ L of IR dye-labeled DNA probe in at least 1 mL of fresh ExpressHyb. Following incubation, membranes were washed sequentially in 2x SSC (0.1% SDS) for 10 min each at room temperature. Signal was detected using a BioRad ChemiDoc MP using either IRDye 680 or IRDye 800 settings.

Nanopore sequencing

Library preparation: Total RNA (1 μ g) was isolated from ~20 fly heads using TRIzol reagent and *in vitro* polyadenylated with E. coli Poly(A) Polymerase (NEB, catalog #M0276S). RNA libraries were prepared from 500ng of polyadenylated RNAs using the PCR-cDNA barcoding kit (Oxford Nanopore Technologies, catalog #: SQK-PCB114.24) according to the manufacturer's instructions. Sequencing was performed using R10.4.1 Flongle flow cells using a MinION Mk1B device for 48 h. Raw signal data were basecalled in real time using the Dorado basecaller integrated in MinKNOW (Dorado version: 7.4.12). Reads were aligned to a single copy of the *Drosophila melanogaster* ribosomal RNA primary transcript using Minimap 2 (Version 2.17-r941) with default parameters for long-read RNA alignment. Processed reads were visualized using IGV (Version 2.12.3) to assess the abundance and integrity of rRNA intermediates.

Nanoblot sequencing quantification: Read counts were obtained using the featureCounts function from Subread software version 2.12.3.⁸⁷ Differential expression analysis and normalization to library size were performed with DESeq2 (v1.38.3).⁸⁸ Nanoblot analysis was used to visualize and quantify the abundance of 2S rRNA extension products for three samples, as described in.⁵²

Brain dissections and immunocytochemistry

Mushroom body staining via anti-Fasciclin II antibody: Brain dissections and immunostaining were performed as described previously.⁸⁶ Brains from anesthetized flies

were dissected in 1x PBS, fixed overnight at 4% paraformaldehyde (Electron Microscopy Sciences, 32% PFA, Cat #15714-S), washed three times in 1x PBS, and permeabilized with 0.3% PBS-Triton. Samples were incubated for two days with primary antibody (1D4 anti-Fasciclin II; 1:20) diluted in antibody solution (0.1% PBS-Triton and Normal Goat Serum (NGS)). Following several washes with 0.1% PBS-Triton, brains were incubated overnight with the appropriate fluorescently conjugated secondary antibody (1:500) in antibody solution overnight at 4°C, washed again, and mounted in ProLong Gold Antifade reagent (Invitrogen). The 1D4 anti-Fasciclin II hybridoma (1:20)⁸⁹ was obtained from the Developmental Studies Hybridoma Bank (DHSB). Imaging was performed using a Zeiss LSM 880 confocal microscope.

Fly brain staining via anti-DLG and anti-GFP antibodies: Brains from anesthetized flies were dissected in ice-cold 0.05% PBS-Triton and fixed overnight at 4°C in 4% paraformaldehyde. Following fixation, brains were washed three times for 1 h each in PBST. Brains were then incubated with primary antibodies diluted in antibody solution (970µL of PBST, 30µL normal goat serum (NGS), 1µL rabbit anti-GFP (Cell Signaling Technology, Cat # 2956S, 1:1000), and 50 µL mouse anti-DLG (1:20)) for 3 h at RT, followed by overnight incubation at 4°C. After three 1-h washes in PBST, samples were incubated with the appropriate fluorescently conjugated secondary antibodies (1:500) in antibody solution for 3 h at RT, and then 3–4 days at 4°C. Brains were washed three more times for 1 h, mounted in ProLong Gold Antifade reagent on slides with coverslip spacers to prevent tissue damage, and imaged at 40X using a Leica SP8 confocal microscope. Confocal max intensity projection images of brain structures were produced using Las X software (Leica Microsystems). Quantification of the region of interest was calculated from the largest section and normalized to WT/WT.

Behavioral assays

Lifespan analysis: Lifespan was measured in standard conditions at 25°C. Newly eclosed flies were collected, separated by sex, and placed in fresh food vials (up to 15 flies per vial). Flies were transferred to new vials weekly, and survivorship was recorded daily for all genotypes. At least 100 flies per genotype were analyzed. Survivorship curves were compared using log rank (Mantel-Cox) test in PRISM (GraphPad, San Diego).

Locomotor function assay: Negative geotaxis assays were performed as described⁹⁰ with minor modifications. Newly eclosed *Rrp40* flies (WT/WT, G11A/G11A, G146C/G146C) were collected on day 0, divided into groups of 12, and housed in separate vials. For each trial, age-matched cohorts were transferred into a 25-mL graduated cylinder, and climbing ability was assessed as described in the assay protocol.

Learning and memory: Tastant-induced proboscis extension learning and memory assays were performed as described^{91,92} to assess taste response and short-term memory in wildtype and mutant flies. Flies were starved for 18 h prior to testing by placing ten flies per vial with only a water-dampened Kim-wipe. Each genotype included six independent groups of 10 flies. To minimize stress-induced behavioral changes, flies were immobilized on ice (rather than CO₂) and mounted onto microscope slides by their wings, allowing only head

mobility. Sucrose stimuli were prepared by twisting the tip of a Kimwipe into a thin thread before dipping it into 500 μ M sucrose solution (EMD, Cat #SX1075–1) to limit solution volume. During the pre-test, sucrose was presented to all flies as a positive control, and any flies that failed to extend their proboscis were excluded. Training consisted of three cycles at 5-min intervals in which flies were sequentially exposed to caffeine deterrent (20 μ M caffeine in dH₂O; (Sigma Aldrich Cat #CO750–500G) followed by the sucrose attractant. Short-term memory was assessed by presenting sucrose immediately after training (0 min) and again at 30 min. Flies with impaired learning and memory exhibited a higher proboscis extension response to sucrose following training compared to controls.

Immunoblotting: Protein lysates (20 μ g) from fly heads were resolved on 4–20% Criterion TGX polyacrylamide gels (BioRad) and transferred to nitrocellulose membranes. Membranes were blocked for 5–10 min in Everyblot Blocking Buffer (BioRad, Cat#12010020) and incubated overnight at 4°C with primary antibodies diluted in blocking buffer. Detection was performed using species-specific horseradish peroxidase (HRP)-conjugated secondary antibodies (Invitrogen) and enhanced chemiluminescence (ECL, Sigma). Primary antibodies include rabbit anti-Rrp40 (custom made with Pacific Immunology), rabbit anti-Arc1 (gift from Dr. Travis Thomson) and mouse anti-GAPDH (1:1000, Proteintech).

QUANTIFICATION AND STATISTICAL ANALYSIS

Statistical analyses and data presentation were constructed using GRAPHPAD Prism 10 (GraphPad Software, San Diego, CA, USA). All results are represented as mean \pm SEM. Statistical significance was determined using either an unpaired *t* test or ordinary one-way ANOVA. For all statistical analyses, differences were considered significant if $p < 0.05$. Confocal microscopy image processing and quantification were performed using Imaris software (Oxford Instruments), with quantification based on the mean maximum fluorescence intensity per sample. –

Supplementary Material

Refer to Web version on PubMed Central for supplementary material.

ACKNOWLEDGMENTS

This work was supported by a National Institutes of Health R01 grant (NS131620), the Alfred P. Sloan Research Fellowship in Neuroscience award (FG-2023-20698), and a University of Southern California-Buck Institute Nathan Shock Center Award (P30AG068345) to D.J.M. L.A.H. was supported by the National Science Foundation Graduate Research Fellowship Program and a University of Southern California Provost Fellowship. B.A.B. was supported by Simons Foundation award SF811217. H.R.S.W. and A.M.R. were supported by a National Institutes of Health R01 grant (NS121550). We also thank Dr. Amber Mosley for her assistance with the analysis of quantitative proteomics data generated for this study.

REFERENCES

1. Doma MK, and Parker R (2007). RNA quality control in eukaryotes. *Cell* 131, 660–668. [PubMed: 18022361]
2. Wolin SL, and Maquat LE (2019). Cellular RNA surveillance in health and disease. *Science* 366, 822–827. [PubMed: 31727827]

3. Laffleur B, and Basu U (2019). Biology of RNA Surveillance in Development and Disease. *Trends Cell Biol.* 29, 428–445. [PubMed: 30755352]
4. Su Z, Fang M, Smolnikov A, Vafae F, Dinger ME, and Oates EC (2024). Post-transcriptional regulation supports the homeostatic expression of mature RNA. *Brief. Bioinform.* 26, bbaf027. [PubMed: 39913622]
5. Schoenberg DR, and Maquat LE (2012). Regulation of cytoplasmic mRNA decay. *Nat. Rev. Genet.* 13, 246–259. [PubMed: 22392217]
6. Garneau NL, Wilusz J, and Wilusz CJ (2007). The highways and byways of mRNA decay. *Nat. Rev. Mol. Cell Biol.* 8, 113–126. [PubMed: 17245413]
7. Duan R, Sharma S, Xia Q, Garber K, and Jin P (2014). Towards understanding RNA-mediated neurological disorders. *J. Genet. Genomics* 41, 473–484. [PubMed: 25269673]
8. Alaqeel AM, Abou Al-Shaar H, Shariff RK, and Albakr A (2015). The role of RNA metabolism in neurological diseases. *Balkan J. Med. Genet.* 18, 5–14.
9. Nussbacher JK, Tabet R, Yeo GW, and Lagier-Tourenne C (2019). Disruption of RNA Metabolism in Neurological Diseases and Emerging Therapeutic Interventions. *Neuron* 102, 294–320. [PubMed: 30998900]
10. Rice GI, Reijns MAM, Coffin SR, Forte GMA, Anderson BH, Szykiewicz M, Gornall H, Gent D, Leitch A, Botella MP, et al. (2013). Synonymous mutations in RNASEH2A create cryptic splice sites impairing RNase H2 enzyme function in Aicardi-Goutieres syndrome. *Hum. Mutat.* 34, 1066–1070. [PubMed: 23592335]
11. Crow YJ, Leitch A, Hayward BE, Garner A, Parmar R, Griffith E, Ali M, Semple C, Aicardi J, Babul-Hirji R, et al. (2006). Mutations in genes encoding ribonuclease H2 subunits cause Aicardi-Goutieres syndrome and mimic congenital viral brain infection. *Nat. Genet.* 38, 910–916. [PubMed: 16845400]
12. Cristini A, Tellier M, Constantinescu F, Accalai C, Albulescu LO, Heiringhoff R, Bery N, Sordet O, Murphy S, and Gromak N (2022). RNase H2, mutated in Aicardi-Goutieres syndrome, resolves co-transcriptional R-loops to prevent DNA breaks and inflammation. *Nat. Commun.* 13, 2961. [PubMed: 35618715]
13. Budde BS, Namavar Y, Barth PG, Poll-The BT, Nürnberg G, Becker C, van Ruissen F, Weterman MAJ, Fluiter K, te Beek ET, et al. (2008). tRNA splicing endonuclease mutations cause pontocerebellar hypoplasia. *Nat. Genet.* 40, 1113–1118. [PubMed: 18711368]
14. Namavar Y, Chitayat D, Barth PG, van Ruissen F, de Wissel MB, Poll-The BT, Silver R, and Baas F (2011). TSEN54 mutations cause pontocerebellar hypoplasia type 5. *Eur. J. Hum. Genet.* 19, 724–726. [PubMed: 21368912]
15. Schaffer AE, Eggens VRC, Caglayan AO, Reuter MS, Scott E, Coufal NG, Silhavy JL, Xue Y, Kayserili H, Yasuno K, et al. (2014). CLP1 founder mutation links tRNA splicing and maturation to cerebellar development and neurodegeneration. *Cell* 157, 651–663. [PubMed: 24766810]
16. Boczonadi V, Müller JS, Pyle A, Munkley J, Dor T, Quartararo J, Ferrero I, Karcagi V, Giunta M, Polvikoski T, et al. (2014). EXOSC8 mutations alter mRNA metabolism and cause hypomyelination with spinal muscular atrophy and cerebellar hypoplasia. *Nat. Commun.* 5, 4287. [PubMed: 24989451]
17. Burns DT, Donkervoort S, Müller JS, Knierim E, Bharucha-Goebel D, Faqieh EA, Bell SK, AlFaifi AY, Monies D, Millan F, et al. (2018). Variants in EXOSC9 Disrupt the RNA Exosome and Result in Cerebellar Atrophy with Spinal Motor Neuronopathy. *Am. J. Hum. Genet.* 102, 858–873. [PubMed: 29727687]
18. Wan J, Yourshaw M, Mamsa H, Rudnik-Schöneborn S, Menezes MP, Hong JE, Leong DW, Senderek J, Salman MS, Chitayat D, et al. (2012). Mutations in the RNA exosome component gene EXOSC3 cause pontocerebellar hypoplasia and spinal motor neuron degeneration. *Nat. Genet.* 44, 704–708. [PubMed: 22544365]
19. Rudnik-Schöneborn S, Senderek J, Jen JC, Houge G, Seeman P, Puchmajerova A, Graul-Neumann L, Seidel U, Korinthenberg R, Kirschner J, et al. (2013). Pontocerebellar hypoplasia type 1: clinical spectrum and relevance of EXOSC3 mutations. *Neurology* 80, 438–446. [PubMed: 23284067]

20. Morton DJ, Kuiper EG, Jones SK, Leung SW, Corbett AH, and Fasken MB (2018). The RNA exosome and RNA exosome-linked disease. *RNA* 24, 127–142. [PubMed: 29093021]
21. Liu Q, Greimann JC, and Lima CD (2006). Reconstitution, activities, and structure of the eukaryotic RNA exosome. *Cell* 127, 1223–1237. [PubMed: 17174896]
22. Mitchell P, Petfalski E, Shevchenko A, Mann M, and Tollervey D (1997). The exosome: a conserved eukaryotic RNA processing complex containing multiple 3'→5' exoribonucleases. *Cell* 91, 457–466. [PubMed: 9390555]
23. Dziembowski A, Lorentzen E, Conti E, and Séraphin B (2007). A single subunit, Dis3, is essentially responsible for yeast exosome core activity. *Nat. Struct. Mol. Biol.* 14, 15–22. [PubMed: 17173052]
24. Januszyk K, and Lima CD (2014). The eukaryotic RNA exosome. *Curr. Opin. Struct. Biol.* 24, 132–140. [PubMed: 24525139]
25. Schneider C, and Tollervey D (2013). Threading the barrel of the RNA exosome. *Trends Biochem. Sci.* 38, 485–493. [PubMed: 23910895]
26. Mitchell P, Petfalski E, and Tollervey D (1996). The 3' end of yeast 5.8S rRNA is generated by an exonuclease processing mechanism. *Genes Dev.* 10, 502–513. [PubMed: 8600032]
27. Januszyk K, and Lima CD (2011). Structural components and architectures of RNA exosomes. *Adv. Exp. Med. Biol.* 702, 9–28. [PubMed: 21713674]
28. Das M, Zattas D, Zinder JC, Wasmuth EV, Henri J, and Lima CD (2021). Substrate discrimination and quality control require each catalytic activity of TRAMP and the nuclear RNA exosome. *Proc. Natl. Acad. Sci. USA* 118, e2024846118. [PubMed: 33782132]
29. Zinder JC, and Lima CD (2017). Targeting RNA for processing or destruction by the eukaryotic RNA exosome and its cofactors. *Genes Dev.* 31, 88–100. [PubMed: 28202538]
30. Kilchert C (2020). RNA Exosomes and Their Cofactors. *Methods Mol. Biol.* 2062, 215–235. [PubMed: 31768979]
31. Zhang L, Wang J, Tang Z, Lin Z, Su R, Hu N, Tang Y, Ge G, Fan J, Tong MH, et al. (2025). The nuclear exosome co-factor MTR4 shapes the transcriptome for meiotic initiation. *Nat. Commun.* 16, 2605. [PubMed: 40097464]
32. Kowalinski E, Kögel A, Ebert J, Reichelt P, Stegmann E, Habermann B, and Conti E (2016). Structure of a Cytoplasmic 11-Subunit RNA Exosome Complex. *Mol. Cell* 63, 125–134. [PubMed: 27345150]
33. Araki Y, Takahashi S, Kobayashi T, Kajihō H, Hoshino S, and Katada T (2001). Ski7p G protein interacts with the exosome and the Ski complex for 3'-to-5' mRNA decay in yeast. *EMBO J.* 20, 4684–4693. [PubMed: 11532933]
34. Lubas M, Christensen MS, Kristiansen MS, Domanski M, Falkenby LG, Lykke-Andersen S, Andersen JS, Dziembowski A, and Jensen TH (2011). Interaction profiling identifies the human nuclear exosome targeting complex. *Mol. Cell* 43, 624–637. [PubMed: 21855801]
35. Fasken MB, Losh JS, Leung SW, Brutus S, Avin B, Vaught JC, Potter-Birriel J, Craig T, Conn GL, Mills-Lujan K, et al. (2017). Insight into the RNA Exosome Complex Through Modeling Pontocerebellar Hypoplasia Type 1b Disease Mutations in Yeast. *Genetics* 205, 221–237. [PubMed: 27777260]
36. Gillespie A, Gabunilas J, Jen JC, and Chanfreau GF (2017). Mutations of EXOSC3/Rrp40p associated with neurological diseases impact ribosomal RNA processing functions of the exosome in *S. cerevisiae*. *RNA* 23, 466–472. [PubMed: 28053271]
37. Slavotinek A, Misceo D, Htun S, Mathisen L, Frengen E, Foreman M, Hurtig JE, Enyenihi L, Sterrett MC, Leung SW, et al. (2020). Biallelic variants in the RNA exosome gene EXOSC5 are associated with developmental delays, short stature, cerebellar hypoplasia and motor weakness. *Hum. Mol. Genet.* 29, 2218–2239. [PubMed: 32504085]
38. Fasken MB, Leung SW, Cureton LA, Al-Awadi M, Al-Kindy A, van Hoof A, Khoshnevis S, Ghalei H, Al-Maawali A, and Corbett AH (2024). A biallelic variant of the RNA exosome gene, EXOSC4, associated with neurodevelopmental defects impairs RNA exosome function and translation. *J. Biol. Chem.* 300, 107571. [PubMed: 39009343]

39. Morton DJ, Jalloh B, Kim L, Kremesky I, Nair RJ, Nguyen KB, Rounds JC, Sterrett MC, Brown B, Le T, et al. (2020). A *Drosophila* model of Pontocerebellar Hypoplasia reveals a critical role for the RNA exosome in neurons. *PLoS Genet.* 16, e1008901. [PubMed: 32645003]
40. Ashley J, Cordy B, Lucia D, Fradkin LG, Budnik V, and Thomson T (2018). Retrovirus-like Gag Protein Arc1 Binds RNA and Traffics across Synaptic Boutons. *Cell* 172, 262–274.e11. [PubMed: 29328915]
41. Zanni G, Scotton C, Passarelli C, Fang M, Barresi S, Dallapiccola B, Wu B, Gualandi F, Ferlini A, Bertini E, and Wei W (2013). Exome sequencing in a family with intellectual disability, early onset spasticity, and cerebellar atrophy detects a novel mutation in EXOSC3. *Neurogenetics* 14, 247–250. [PubMed: 23975261]
42. Halevy A, Lerer I, Cohen R, Kornreich L, Shuper A, Gamliel M, Zimerman BE, Korabi I, Meiner V, Straussberg R, and Lossos A (2014). Novel EXOSC3 mutation causes complicated hereditary spastic paraplegia. *J. Neurol.* 261, 2165–2169. [PubMed: 25149867]
43. Li H, Janssens J, De Waegeneer M, Kolluru SS, Davie K, Gardeux V, Saelens W, David FPA, Brbi M, Spanier K, et al. (2022). Fly Cell Atlas: A single-nucleus transcriptomic atlas of the adult fruit fly. *Science* 375, eabk2432. [PubMed: 35239393]
44. Li H (2021). Single-cell RNA sequencing in *Drosophila*: Technologies and applications. *Wiley Interdiscip. Rev. Dev. Biol.* 10, e396. [PubMed: 32940008]
45. Davie K, Janssens J, Koldere D, De Waegeneer M, Pech U, Kreft L, Aibar S, Makhzami S, Christiaens V, Bravo González-Blas C, et al. (2018). A Single-Cell Transcriptome Atlas of the Aging *Drosophila* Brain. *Cell* 174, 982–998.e20. [PubMed: 29909982]
46. Croset V, Treiber CD, and Waddell S (2018). Cellular diversity in the *Drosophila* midbrain revealed by single-cell transcriptomics. *eLife* 7, e34550. [PubMed: 29671739]
47. Barnstedt O, Oswald D, Felsenberg J, Brain R, Moszynski JP, Talbot CB, Perrat PN, and Waddell S (2016). Memory-Relevant Mushroom Body Output Synapses Are Cholinergic. *Neuron* 89, 1237–1247. [PubMed: 26948892]
48. Briggs MW, Burkard KT, and Butler JS (1998). Rrp6p, the yeast homologue of the human PM-Scl 100-kDa autoantigen, is essential for efficient 5.8 S rRNA 3' end formation. *J. Biol. Chem.* 273, 13255–13263. [PubMed: 9582370]
49. Miller BR, Wei T, Fields CJ, Sheng P, and Xie M (2018). Near-infrared fluorescent northern blot. *RNA* 24, 1871–1877. [PubMed: 30201850]
50. Long EO, and Dawid IB (1980). Alternative pathways in the processing of ribosomal RNA precursor in *Drosophila melanogaster*. *J. Mol. Biol.* 138, 873–878. [PubMed: 6774101]
51. Gerstberger S, Meyer C, Benjamin-Hong S, Rodriguez J, Briskin D, Bognanni C, Bogardus K, Steller H, and Tuschl T (2017). The Conserved RNA Exonuclease Rexo5 Is Required for 3' End Maturation of 28S rRNA, 5S rRNA, and snoRNAs. *Cell Rep.* 21, 758–772. [PubMed: 29045842]
52. DeMario S, Xu K, He K, and Chanfreau GF (2023). Nanoblot: an R-package for visualization of RNA isoforms from long-read RNA-sequencing data. *RNA* 29, 1099–1107. [PubMed: 37137666]
53. Hulse BK, Haberkern H, Franconville R, Turner-Evans D, Takemura SY, Wolff T, Noorman M, Dreher M, Dan C, Parekh R, et al. (2021). A connectome of the *Drosophila* central complex reveals network motifs suitable for flexible navigation and context-dependent action selection. *eLife* 10, e66039. [PubMed: 34696823]
54. Lin S (2023). The making of the *Drosophila* mushroom body. *Front. Physiol.* 14, 1091248. [PubMed: 36711013]
55. de Belle JS, and Heisenberg M (1994). Associative odor learning in *Drosophila* abolished by chemical ablation of mushroom bodies. *Science* 263, 692–695. [PubMed: 8303280]
56. Miller SA, Policastro RA, Sriramkumar S, Lai T, Huntington TD, Ladaika CA, Kim D, Hao C, Zentner GE, and O'Hagan HM (2021). LSD1 and Aberrant DNA Methylation Mediate Persistence of Enteroendocrine Progenitors That Support BRAF-Mutant Colorectal Cancer. *Cancer Res.* 81, 3791–3805. [PubMed: 34035083]
57. McBride SM, Giuliani G, Choi C, Krause P, Correale D, Watson K, Baker G, and Siwicki KK (1999). Mushroom body ablation impairs short-term memory and long-term memory of courtship conditioning in *Drosophila melanogaster*. *Neuron* 24, 967–977. [PubMed: 10624959]

58. Martin JR, Ernst R, and Heisenberg M (1998). Mushroom bodies suppress locomotor activity in *Drosophila melanogaster*. *Learn. Mem.* 5, 179–191. [PubMed: 10454382]
59. Strauss R (2002). The central complex and the genetic dissection of locomotor behaviour. *Curr. Opin. Neurobiol.* 12, 633–638. [PubMed: 12490252]
60. Robinow S, and White K (1988). The locus *elav* of *Drosophila melanogaster* is expressed in neurons at all developmental stages. *Dev. Biol.* 126, 294–303. [PubMed: 3127258]
61. Pastuzyn ED, Day CE, Kearns RB, Kyrke-Smith M, Taibi AV, Mc-Cormick J, Yoder N, Belnap DM, Erlendsson S, Morado DR, et al. (2018). The Neuronal Gene *Arc* Encodes a Repurposed Retrotransposon Gag Protein that Mediates Intercellular RNA Transfer. *Cell* 173, 275–288.e18. [PubMed: 29570995]
62. Lu B, and Vogel H (2009). *Drosophila* models of neurodegenerative diseases. *Annu. Rev. Pathol.* 4, 315–342. [PubMed: 18842101]
63. West S, Gromak N, and Proudfoot NJ (2004). Human 5' → 3' exonuclease *Xrn2* promotes transcription termination at co-transcriptional cleavage sites. *Nature* 432, 522–525. [PubMed: 15565158]
64. Gudipati RK, Xu Z, Lebreton A, Séraphin B, Steinmetz LM, Jacquier A, and Libri D (2012). Extensive degradation of RNA precursors by the exosome in wild-type cells. *Mol. Cell* 48, 409–421. [PubMed: 23000176]
65. Showell SS, Martinez Y, Gondolfo S, Boppana S, and Lawal HO (2020). Overexpression of the vesicular acetylcholine transporter disrupts cognitive performance and causes age-dependent locomotion decline in *Drosophila*. *Mol. Cell. Neurosci.* 105, 103483. [PubMed: 32217162]
66. Teber I, Köhling R, Speckmann EJ, Barnekow A, and Kremerskothen J (2004). Muscarinic acetylcholine receptor stimulation induces expression of the activity-regulated cytoskeleton-associated gene (*ARC*). *Brain Res. Mol. Brain Res.* 121, 131–136. [PubMed: 14969744]
67. White D, de Sousa Abreu RP, Blake A, Murphy J, Showell S, Kitamoto T, and Lawal HO (2020). Deficits in the vesicular acetylcholine transporter alter lifespan and behavior in adult *Drosophila melanogaster*. *Neurochem. Int.* 137, 104744. [PubMed: 32315665]
68. Chen ZR, Huang JB, Yang SL, and Hong FF (2022). Role of Cholinergic Signaling in Alzheimer's Disease. *Molecules* 27, 1816. [PubMed: 35335180]
69. Muller ML, and Bohnen NI (2013). Cholinergic dysfunction in Parkinson's disease. *Curr. Neurol. Neurosci. Rep.* 13, 377. [PubMed: 23943367]
70. Smith R, Chung H, Rundquist S, Maat-Schieman MLC, Colgan L, Englund E, Liu YJ, Roos RAC, Faull RLM, Brundin P, and Li JY (2006). Cholinergic neuronal defect without cell loss in Huntington's disease. *Hum. Mol. Genet.* 15, 3119–3131. [PubMed: 16987871]
71. Bhat VD, Jayaraj J, and Babu K (2022). RNA and neuronal function: the importance of post-transcriptional regulation. *Oxf. Open Neurosci.* 1, kvac011. [PubMed: 38596700]
72. Landinez-Macias M, and Urwyler O (2021). The Fine Art of Writing a Message: RNA Metabolism in the Shaping and Remodeling of the Nervous System. *Front. Mol. Neurosci.* 14, 755686. [PubMed: 34916907]
73. Schulz L, Ramirez P, Lemieux A, Gonzalez E, Thomson T, and Frost B (2023). Tau-Induced Elevation of the Activity-Regulated Cytoskeleton Associated Protein *Arc1* Causally Mediates Neurodegeneration in the Adult *Drosophila* Brain. *Neuroscience* 518, 101–111. [PubMed: 35487302]
74. Hao Y, Stuart T, Kowalski MH, Choudhary S, Hoffman P, Hartman A, Srivastava A, Molla G, Madad S, Fernandez-Granda C, and Satija R (2024). Dictionary learning for integrative, multimodal and scalable single-cell analysis. *Nat. Biotechnol.* 42, 293–304. [PubMed: 37231261]
75. Butler A, Hoffman P, Smibert P, Papalexi E, and Satija R (2018). Integrating single-cell transcriptomic data across different conditions, technologies, and species. *Nat. Biotechnol.* 36, 411–420. [PubMed: 29608179]
76. Stuart T, Butler A, Hoffman P, Hafemeister C, Papalexi E, Mauck WM 3rd, Hao Y, Stoeckius M, Smibert P, and Satija R (2019). Comprehensive Integration of Single-Cell Data. *Cell* 177, 1888–1902.e21. [PubMed: 31178118]
77. Li H (2018). *Minimap2*: pairwise alignment for nucleotide sequences. *Bioinformatics* 34, 3094–3100. [PubMed: 29750242]

78. Robinson JT, Thorvaldsdóttir H, Winckler W, Guttman M, Lander ES, Getz G, and Mesirov JP (2011). Integrative genomics viewer. *Nat. Biotechnol.* 29, 24–26. [PubMed: 21221095]
79. Teefy BB, Adler A, Bhala R, and Benayoun BA (2022). Gentle Isolation of Nuclei from the Brain Tissue of Adult African Turquoise Killifish, a Naturally Short-Lived Model for Aging Research. *J. Vis. Exp.* 186, e64165. 10.3791/64165.
80. McLaughlin CN, Qi Y, Quake SR, Luo L, and Li H (2022). Isolation and RNA sequencing of single nuclei from *Drosophila* tissues. *STAR Protoc.* 3, 101417. [PubMed: 35620068]
81. Zheng GXY, Terry JM, Belgrader P, Ryvkin P, Bent ZW, Wilson R, Ziraldo SB, Wheeler TD, McDermott GP, Zhu J, et al. (2017). Massively parallel digital transcriptional profiling of single cells. *Nat. Commun.* 8, 14049. [PubMed: 28091601]
82. Kuleshov MV, Jones MR, Rouillard AD, Fernandez NF, Duan Q, Wang Z, Koplev S, Jenkins SL, Jagodnik KM, Lachmann A, et al. (2016). Enrichr: a comprehensive gene set enrichment analysis web server 2016 update. *Nucleic Acids Res.* 44, W90–W97. [PubMed: 27141961]
83. Kuleshov MV, Diaz JEL, Flamholz ZN, Keenan AB, Lachmann A, Wojciechowicz ML, Cagan RL, and Ma'ayan A (2019). modEnrichr: a suite of gene set enrichment analysis tools for model organisms. *Nucleic Acids Res.* 47, W183–W190. [PubMed: 31069376]
84. Chen EY, Tan CM, Kou Y, Duan Q, Wang Z, Meirelles GV, Clark NR, and Ma'ayan A (2013). Enrichr: interactive and collaborative HTML5 gene list enrichment analysis tool. *BMC Bioinf.* 14, 128.
85. McCracken NA, Liu H, Runnebohm AM, Wijeratne HRS, Wijeratne AB, Staschke KA, and Mosley AL (2023). Obtaining Functional Proteomics Insights From Thermal Proteome Profiling Through Optimized Melt Shift Calculation and Statistical Analysis With InflectSSP. *Mol. Cell. Proteomics* 22, 100630. [PubMed: 37562535]
86. Wu JS, and Luo L (2006). A protocol for dissecting *Drosophila melanogaster* brains for live imaging or immunostaining. *Nat. Protoc.* 1, 2110–2115. [PubMed: 17487202]
87. Liao Y, Smyth GK, and Shi W (2014). featureCounts: an efficient general purpose program for assigning sequence reads to genomic features. *Bioinformatics* 30, 923–930. [PubMed: 24227677]
88. Love MI, Huber W, and Anders S (2014). Moderated estimation of fold change and dispersion for RNA-seq data with DESeq2. *Genome Biol.* 15, 550. [PubMed: 25516281]
89. Grenningloh G, Rehm EJ, and Goodman CS (1991). Genetic analysis of growth cone guidance in *Drosophila*: fasciclin II functions as a neuronal recognition molecule. *Cell* 67, 45–57. [PubMed: 1913818]
90. Pak C, Garshasbi M, Kahrizi K, Gross C, Apponi LH, Noto JJ, Kelly SM, Leung SW, Tzschach A, Behjati F, et al. (2011). Mutation of the conserved polyadenosine RNA binding protein, ZC3H14/dNab2, impairs neural function in *Drosophila* and humans. *Proc. Natl. Acad. Sci. USA* 108, 12390–12395. [PubMed: 21734151]
91. Li Q, DeBeaubien NA, Sokabe T, and Montell C (2020). Temperature and Sweet Taste Integration in *Drosophila*. *Curr. Biol.* 30, 2207–2209. [PubMed: 32516604]
92. Wang Z, Singhvi A, Kong P, and Scott K (2004). Taste representations in the *Drosophila* brain. *Cell* 117, 981–991. [PubMed: 15210117]

Highlights

- Pathogenic *Rrp40* mutations disrupt RNA exosome function in the fly brain
- Single-nucleus RNA-seq reveals cell-type-specific transcriptome dysregulation
- *Arc1* is broadly misregulated across neuronal and glial populations
- Provides a cell-type-resolved brain atlas for probing RNA surveillance and decay mechanisms

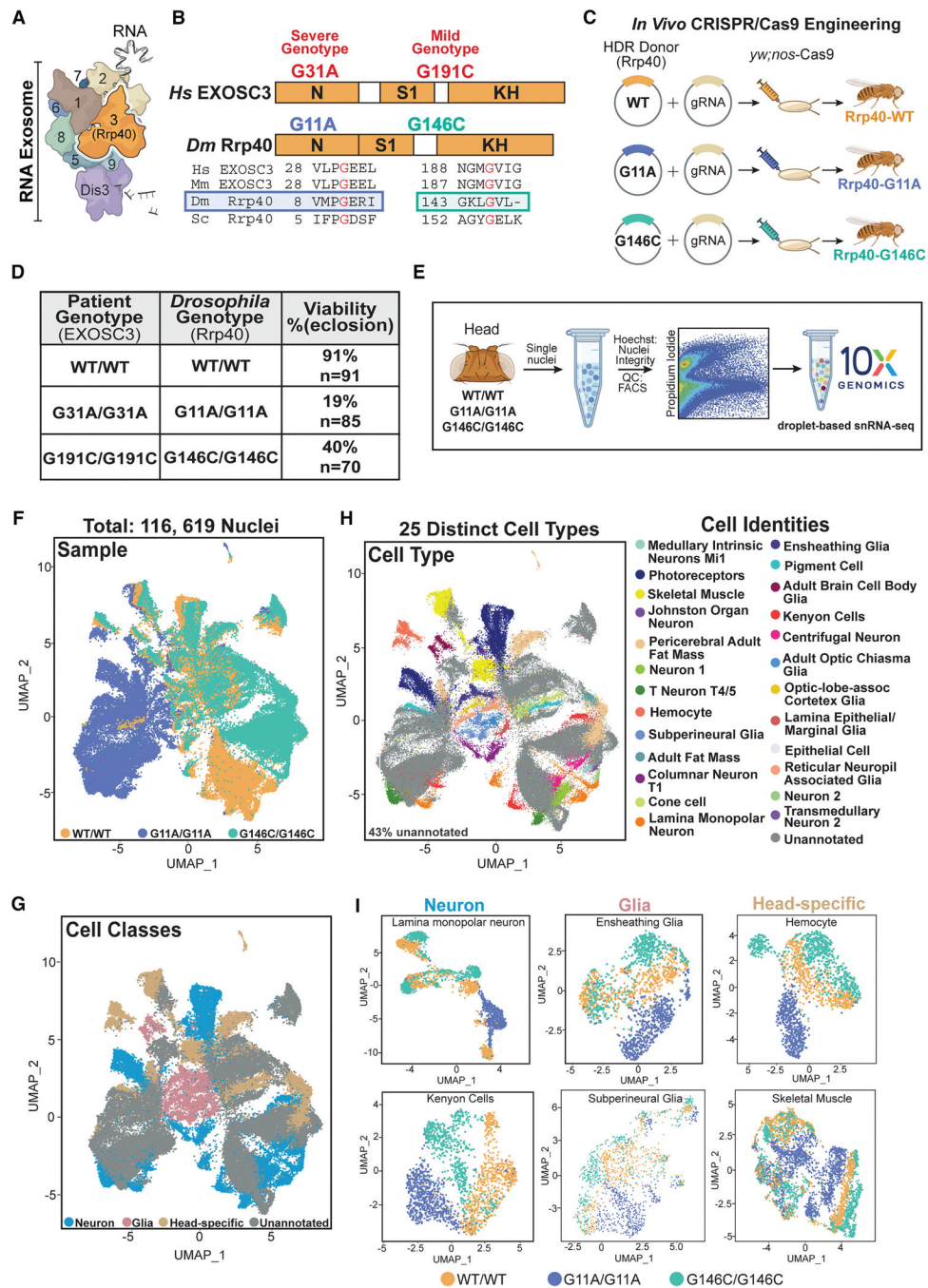


Figure 1. Single-nucleus transcriptome analysis of *Rrp40* mutants reveals distinct cell-type-specific molecular signatures

(A) Illustration of the RNA exosome, an evolutionarily conserved ribonuclease complex composed of structural subunits (EXOSC1–9; EXOSC4 not shown) and a catalytic subunit (Dis3).

(B) Pathogenic variants in EXOSC3 (orange, labeled with “3,” termed Rrp40 in *Drosophila*) cause pontocerebellar hypoplasia type 1b (PCH1b). Domain structures of human EXOSC3 and fly Rrp40 proteins highlight the conservation and disease-associated amino acid changes (in red). Sequence alignments from human, mouse, *Drosophila*, and yeast show conserved

regions surrounding the disease-linked residues. Variants modeled in this study map to the N-terminal (N) and S1 RNA-binding domains of EXOSC3.

(C) Schematic of CRISPR-Cas9 genome-editing strategy used to generate *Rrp40* mutant fly models of EXOSC3-linked PCH1b amino acid substitutions.

(D) Chart of patient genotypes located in *EXOSC3*, the *Drosophila* equivalent genotype in *Rrp40*, and the viability of homozygous *Rrp40* wild-type (WT) and mutant flies modeling PCH1b-linked recessive genotypes (WT/WT, G11A/G11A, and G146C/G146C) shown as %eclosion relative to expected Mendelian ratios. *n* = number of individual flies analyzed.

(E) Experimental design for snRNA-seq study. For each genotype (WT/WT, G11A/G11A, and G146C/G146C), two biological replicates of 20 newly eclosed (day 1) adult female fly heads were pooled. Tissues were dissociated to isolate nuclei, followed by flow cytometry for quality. Libraries were prepared using the 10× Genomics Chromium Next GEM Single Cell 3' kit, targeting 20,000 nuclei per sample.

(F) 2D uniform manifold approximation and projection (UMAP) for dimension reduction of integrated snRNA-seq data from ~116,619 nuclei derived from brain-enriched tissue of age-matched *Rrp40* WT (WT/WT; yellow) and mutant (G11A/G11A, blue; G146C/G146C, teal) flies.

(G) 2D UMAPs colored by broad cell classes (neurons, blue; glia, pink; head specific, tan; unannotated, gray), separated by genotype. Based on the integrated UMAP in (F).

(H) 2D UMAPs colored by 25 cell types (right), separated by genotype. Based on the integrated UMAP in (F).

(I) UMAPs of subclustered neuron, glial, and head-specific cell classes, each colored by genotype (WT/WT, yellow; G11A/G11A, blue; G146C/G146C, tan), highlighting distinct transcriptomic profiles in *Rrp40* mutant flies.

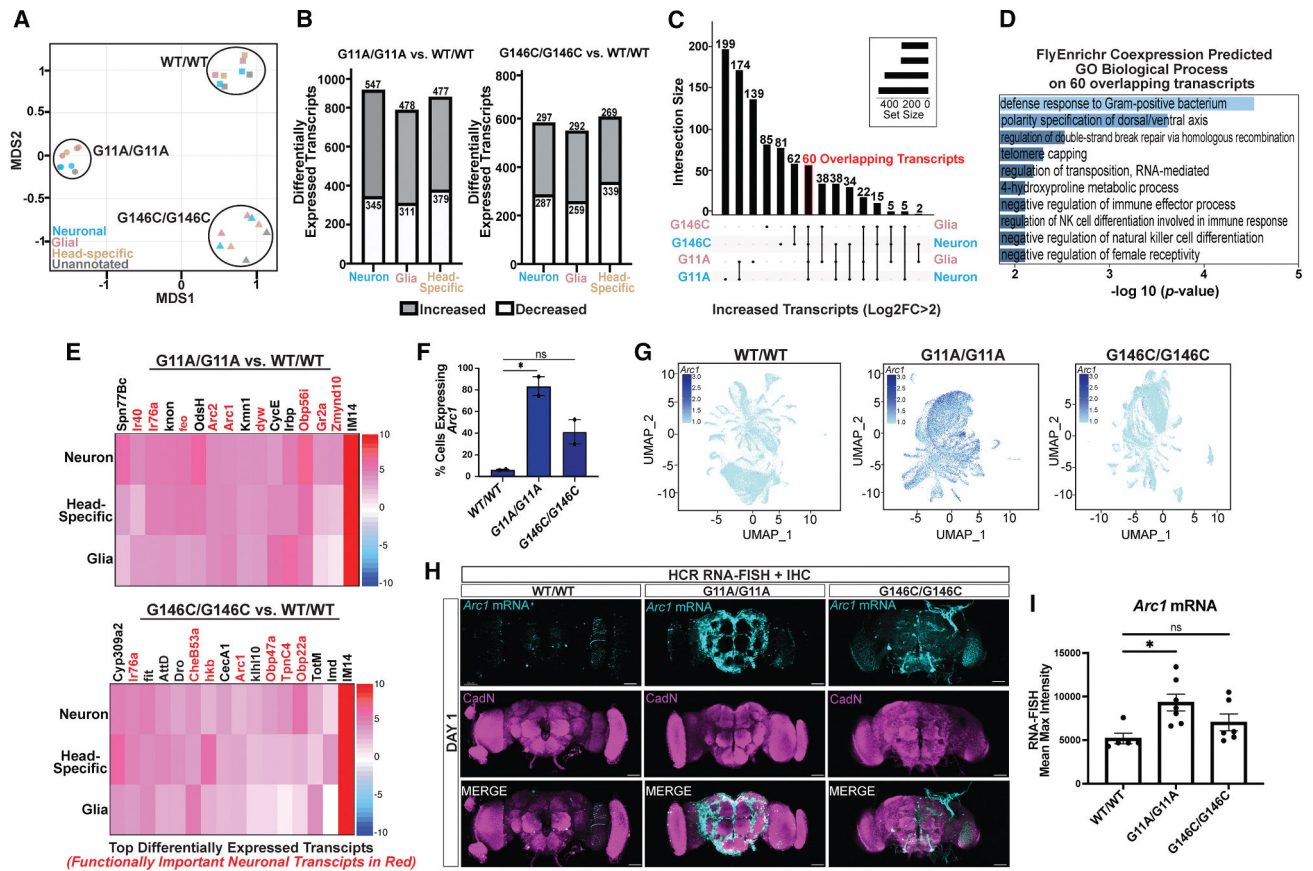


Figure 2. *Rrp40* mutations cause widespread transcriptomic alterations across the brain
 (A) Multidimensional scaling (MDS) plot of snRNA-seq data, with each point colored by cell class (neuronal, blue; glial, pink; head specific, tan; unannotated, gray) and separated by genotype (WT/WT, square; G11A/G11A, circle; and G146C/G146C, triangle).
 (B) Bar graphs showing the number of differentially expressed transcripts increased (gray; log₂ fold change [log₂FC] > 2, FDR < 0.05) or decreased (white, log₂FC < -2, FDR < 0.05) in each genotype compared to WT/WT. Left, G11A/G11A vs. WT/WT; right, G146C/G146C vs. WT/WT. Bars are colored by cell class (neuron, blue; glia, pink; and head specific, tan).
 (C) UpSet plot showing the overall increased differentially expressed transcripts (log₂FC > 2, FDR < 0.05) in neurons (blue) and glia (pink) in G11A/G11A and G146C/G146C mutants compared to WT/WT. A red box highlights 60 transcripts shared between genotypes and cell classes.
 (D) GO biological process enrichment (FlyEnrichr) for the 60 overlapping transcripts in (C), integrated across neuronal and glial subpopulations in both mutants relative to WT/WT. The bars in blue represent significant enrichment (adjusted *p* value < 0.05), ordered by significance.
 (E) Heatmap of the differentially expressed transcripts in G11A/G11A (top) and G146C/G146C (bottom) relative to WT/WT. Functionally important neuronal transcripts are highlighted in red. Normalized log₂FC is shown on a gradient from +10 (red) to -10 (blue).

(F) Quantification of the percentage of cells that express *Arc1* in each *Rrp40* mutant (G11A/G11A or G146C/G146C) and WT control (WT/WT) from the FeaturePlot (G). Results are presented as mean \pm standard error of the mean (SEM) for $n = 2$ biological replicates (ns, not statistically significant and $*p < 0.05$).

(G) 2D UMAP FeaturePlots of *Arc1*-expressing cells (blue) in WT/WT (left), G11/G11A (middle), and G146C/G146C (right) brains. The color gradient from blue to teal indicates high to low expression. Data are from two pooled biological replicates per genotype.

(H) Hybridization chain reaction RNA-FISH (HCR RNA-FISH) of *Arc1* mRNA (teal) combined with immunohistochemistry (magenta; neuropil marker CadN/cadherin) in day 1 whole-mount fly brains. Rows: *Arc1* mRNA (top), CadN (middle), and merged images (bottom). Scale bars, 50 μm . Cadherin staining is shown only to provide spatial context within the brain.

(I) Quantification of mean maximum *Arc1* mRNA fluorescence intensity from *Rrp40* mutant and control brains ($n = 6$) in (H). Values represent the mean \pm SEM ($*p < 0.05$, statistically significant; ns, not significant).

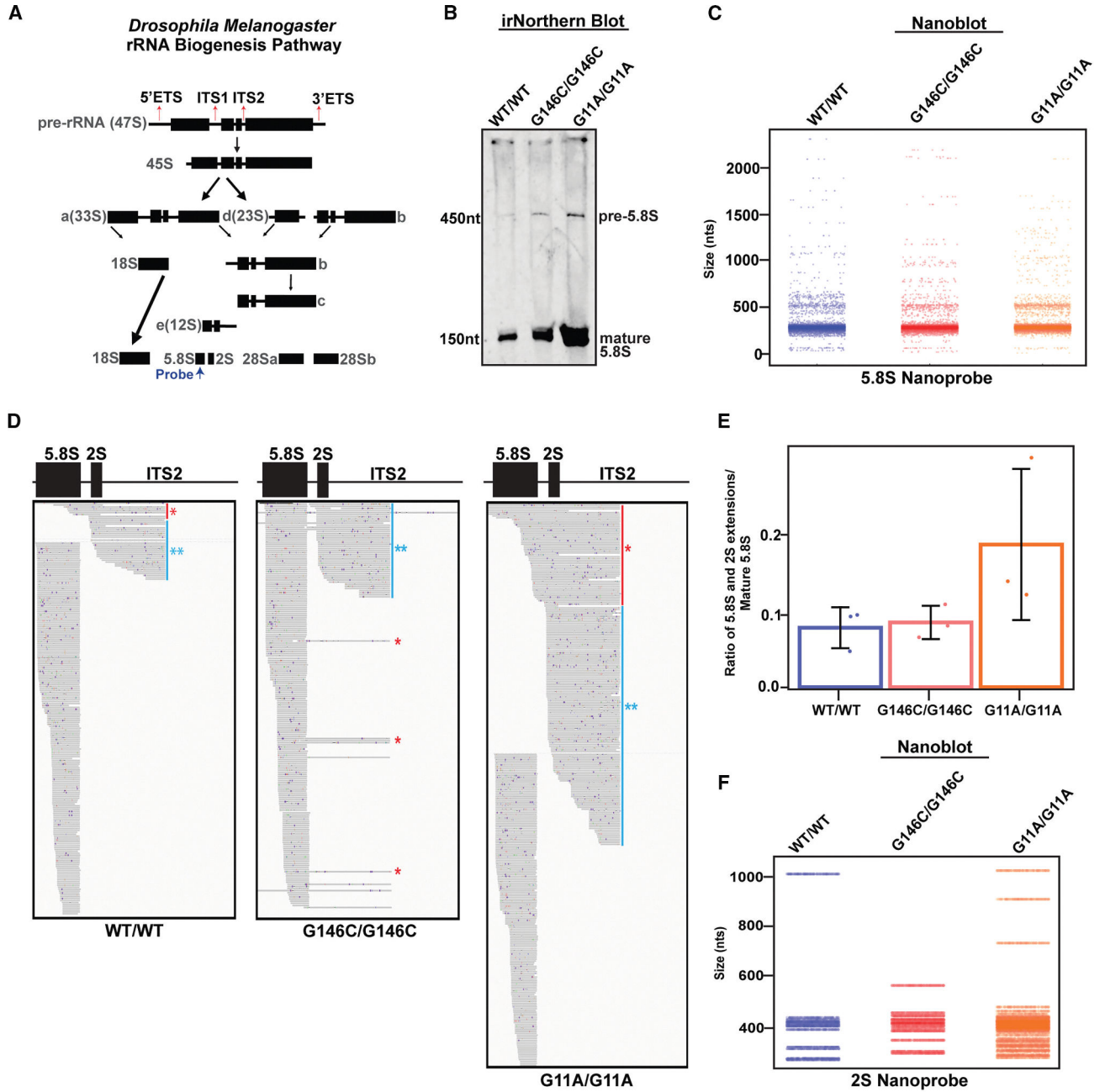


Figure 3. Nanopore long-read sequencing in *Rrp40* mutant head tissue reveals rRNA biogenesis defects

(A) Overview of the *Drosophila melanogaster* ribosomal RNA (rRNA) biogenesis pathway.^{50,51} The sizes of rRNA intermediates are indicated in dark gray. Red arrows denote external or internal spacer regions, which are cleaved and excised to produce mature 18S, 5.8S, 2S, 28Sa, and 28Sb rRNA. A 5.8S probe (dark blue arrow) was used in near-infrared northern (irNorthern) blots in this study.

(B) irNorthern blot analysis of 5.8S rRNAs in brain-enriched tissue from *Rrp40* mutants and WT controls.

(C) “Nanoblot” generated by targeting mature 5.8S rRNA with a 5.8S nanoprobe using Nanopore-based RNA sequencing data from *Rrp40* mutants and WT controls. Note the similarity to the irNorthern blot in (B).

(D) IGV browser screenshots showing single-track read coverage mapping to 5.8S rRNA, 2S rRNA, and ITS2 in *Rrp40* mutants and WT controls. The blue asterisk (*) labels 5.8S species extending into ITS2, while the red asterisk (*) denotes 2S-ITS2 transcripts resulting from impaired degradation.

(E) Quantification of the ratio of extended 5.8S rRNA and 2S rRNA species to mature 5.8S in *Rrp40* mutants and WT controls, shown as a bar graph. Values represent the mean \pm SD for 3 biological replicates.

(F) Nanoblot generated by targeting mature 2S rRNA with a 2S nanoprobe using the Nanopore-based RNA sequencing data from *Rrp40* mutants and WT controls.

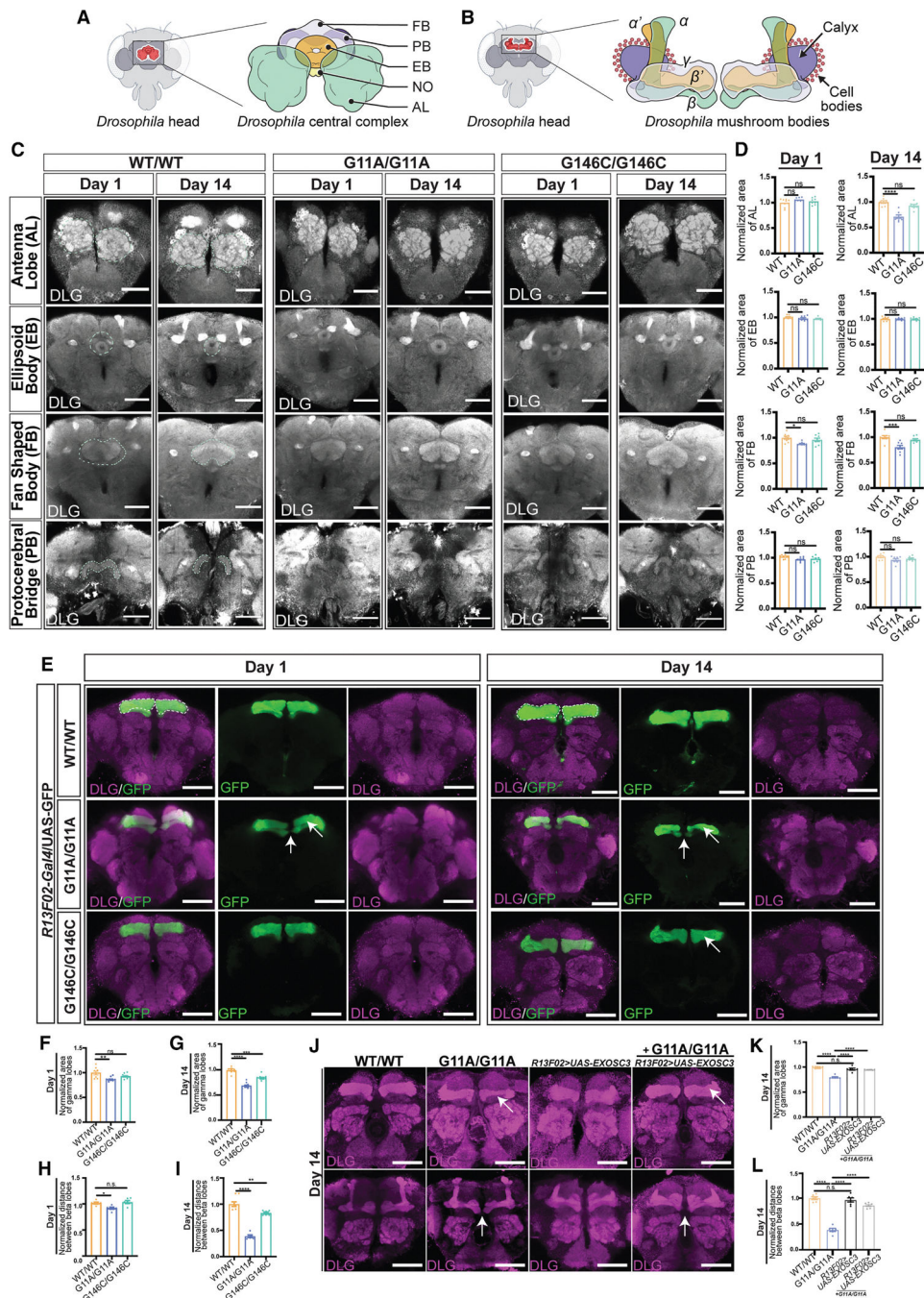


Figure 4. The Rrp40 subunit of the RNA exosome is required for central complex and mushroom body homeostasis within the fly brain

(A) Schematic of the *Drosophila* central complex (left) and the mushroom body (right). The central complex structures highlighted include the fan-shaped body (FB; light purple), protocerebral bridge (PB; dark purple; dorsal to FB), ellipsoid body (EB; orange), noduli (NOs; yellow), and antennae lobes (ALs; green). (B) Mushroom-body structures include vertical α - (orange) and α' - (light green) lobes, medially projecting β - (orange) and β' - (light green) lobes, γ -lobes (light purple), the calyx (dark purple), and Kenyon cell bodies (red).

(C) Confocal max intensity projection images of central complex structures labeled with anti-DLG antibody in WT (WT/WT) and *Rrp40* mutant (G11A/G11A or G146C/G146C) brains from newly eclosed (day 1) or aged (day 14) flies. Single coronal sections show (from top to bottom) ALs, EB, FB, and PB. The columns represent WT/WT (left), G11A/G11A (middle), and G146C/G146C (right) for each age group ($n = 10$ per genotype and age). The region of interest is outlined in green. Scale bar, 100 μm .

(D) Quantification of central complex structures region of interest area from DLG labeling in day 1 and 14 brains from WT/WT and *Rrp40* mutants, normalized to WT/WT values. The data correspond to images in (C). Values represent the mean \pm SD. * $p < 0.05$, ** $p < 0.01$, *** $p < 0.001$, **** $p < 0.0001$, and ns, not significant.

(E) Confocal images of mushroom bodies in WT/WT (top), G11A/G11A (middle), and G146C/G146C (bottom) flies expressing GFP under UAS control in combination with the *R13F02-Gal4* driver (*R13F02-Gal4 > UAS-GFP*) on days 1 (left) and 14 (right) from WT/WT (top row), G11A/G11A (middle row), and G146C/G146C (bottom row) flies on days 1 (left) and 14 (right). The brains were co-labeled with anti-GFP (mushroom-body γ -lobe neurons; green) and anti-DLG (central complex; magenta). Columns: merged GFP/DLG (left), GFP alone (middle), and DLG alone (right). The region of interest is outlined in white. Scale bars, 50 μm .

(F and G) Quantification of γ -lobe region of interest size from GFP labeling on days 1 (F) and 14 (G) in WT/WT and *Rrp40* mutants, based on images in (E). Thinned γ -lobes are indicated by white arrows. The areas of the gamma lobes were normalized to WT/WT controls. Values represent the mean \pm SD. * $p < 0.05$, ** $p < 0.01$, *** $p < 0.001$, **** $p < 0.0001$, and ns, not significant.

(H and I) Quantification of normalized distances between beta lobes on days 1 (H) and 14 (I) in WT/WT and *Rrp40* mutants, based on images in (E). The beta lobe midline is indicated by white arrows. The distance between beta lobes were normalized to WT/WT controls. Values represent the mean \pm SD. * $p < 0.05$, ** $p < 0.01$, **** $p < 0.0001$, and ns, not significant.

(J) Human EXOSC3 (fly *Rrp40*) rescue experiment. Confocal images of day 14 brains from WT, G11A/G11A, *w¹¹¹⁸* flies expressing *UAS-EXOSC3-myc* in mushroom bodies (+/+; *R13F02-Gal4 > UAS-EXOSC3-myc*), and G11A/G11A mutants expressing *UAS-EXOSC3-myc* in the mushroom bodies (G11A/G11A;*R13F02-Gal4 > UAS-EXOSC3-myc*) are included. The brains were labeled with anti-DLG (central complex, magenta). Anti-DLG labeling highlights β -lobe midline-crossing defects in G11A/G11A mutants that are rescued by *EXOSC3* expression (white arrows). Scale bar, 50 μm .

(K and L) Quantification of γ -lobe size (K) and β -lobe midline distance (L) in day 14 WT/WT, G11A/G11A, *w¹¹¹⁸* with *R13F02-Gal4 > UAS-EXOSC3-myc*, and G11A/G11A mutants with *EXOSC3* rescue in mushroom bodies (*G11A/G11A;R13F02-Gal4 > UAS-EXOSC3-myc*). Values represent the mean \pm SD. **** $p < 0.0001$ and ns, not significant.

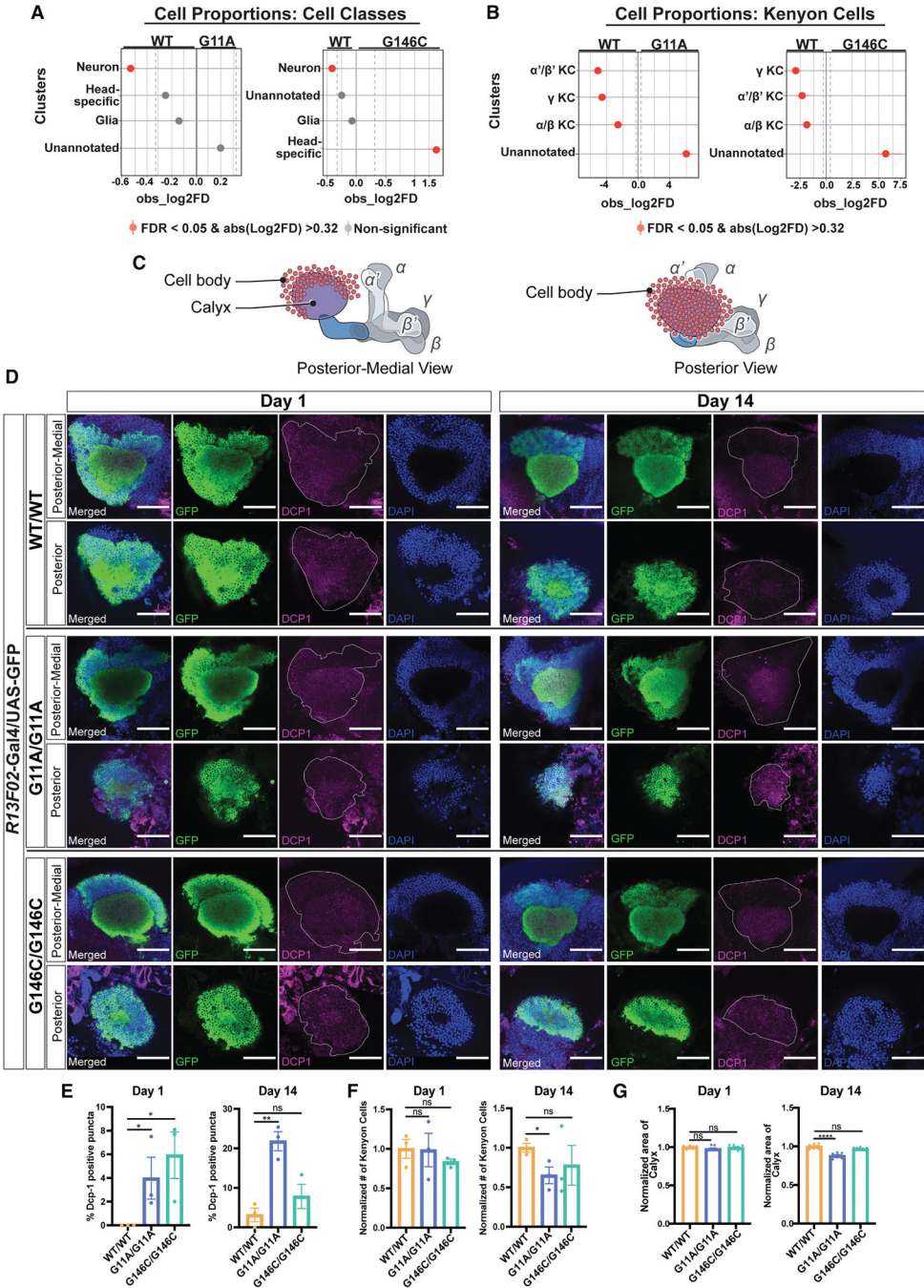


Figure 5. *Rrp40* mutants exhibit neuronal loss within the brain

(A and B) Cellular proportion analysis from the snRNA-seq dataset showing broad cell types (neuron, glia, head specific, and unannotated) (A) and distinct mushroom-body Kenyon cell neuron subtypes ($\alpha\beta$, $\alpha' \beta'$, and γ) (B) in *Rrp40* mutants (G11A/G11A or G146C/G146C) compared to WT controls (WT/WT). In the plots, clusters more abundant in WT/WT are shown on the left, and clusters more abundant in *Rrp40* mutants are shown on the right. The red dots indicate statistically significant differences (FDR < 0.05 and $|\log_2$ fold difference| > 0.32), and the gray dots indicate non-significant differences.

(C) Diagram of the mushroom-body Kenyon cells (red) and calyx (purple) from the posterior-medial and posterior views.

(D) Representative confocal z-projections from posterior-medial and posterior views of WT/WT (top two rows), G11A/G11A (middle two rows), and G146C/G146C (bottom two rows) brains expressing GFP under UAS control in combination with mushroom-body driver (*R13F02-Gal4*) (*R13F02-Gal4>UAS-GFP*). The brains were labeled with anti-GFP (cell bodies and calyx; green), anti-DCP-1 (magenta), and DAPI (blue). Regions of interest for the cell body and calyx are outlined in white. Images are shown for newly eclosed (day 1, left) and aged (day 14, right) flies. Scale bar, 100 μm .

(E–G) Quantification of percentage of DCP-1-positive puncta. Values represent the mean \pm SD. (E), normalized Kenyon cell body numbers (posterior view) (F), and normalized calyx area (G) in WT/WT and *Rrp40* mutant flies on days 1 and 14. * $p < 0.05$, ** $p < 0.01$, **** $p < 0.0001$, and ns, not significant.

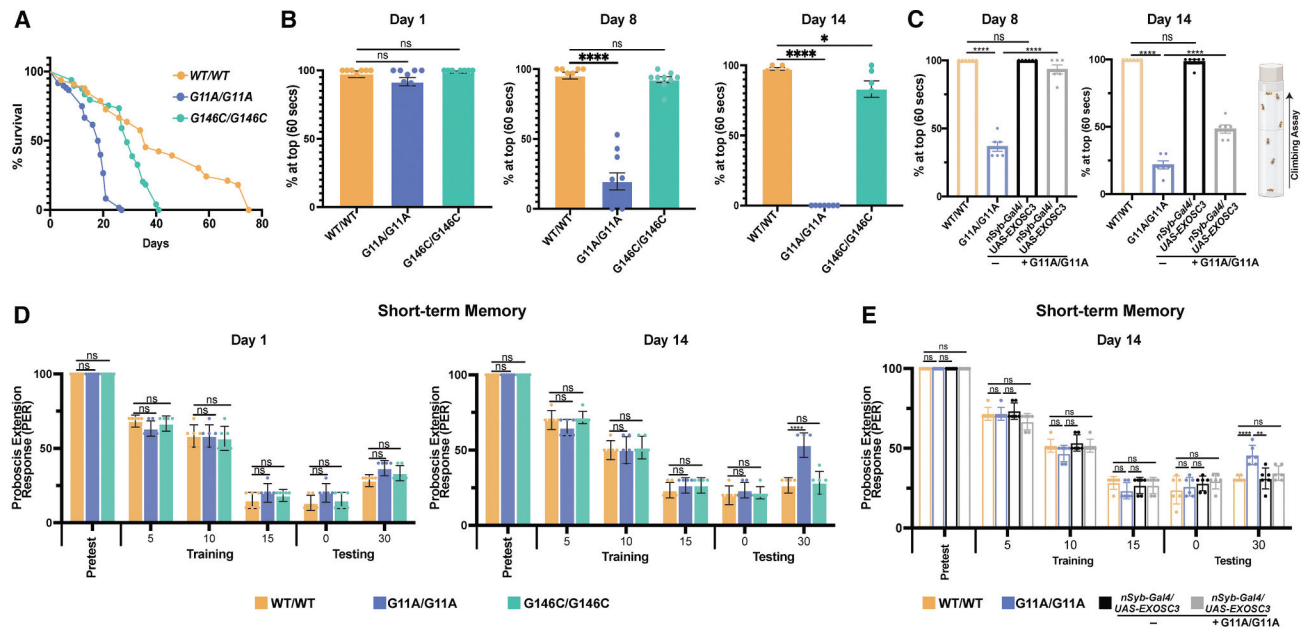


Figure 6. *Rrp40* mutants show a range of organismal and short-term taste memory defects

(A) A Kaplan-Meier survival analysis of WT/WT (tan), *G11A/G11A* (blue), and *G146C/G146C* (green) flies ($n = 100$ per genotype).

(B) Locomotor activity measured by negative geotaxis assay (right, schematic of climbing assay). Data are shown as the mean percentage of flies reaching the top of a cylinder within 60 s, averaged across all trials. Groups of age-matched (days 1, 8, and 14; $n = 36$, cohorts of 9–12 flies) were tested in at least three independent trials per genotype. The results are represented as the mean \pm SEM (ns $p > 0.05$, $*p < 0.05$, and $****p < 0.0001$; unpaired two-tailed t test vs. WT).

(C) Pan-neuronal expression of human *EXOSC3* ($nSyb-Gal4 > UAS-EXOSC3$) significantly rescues locomotor deficits in *Rrp40 G11A/G11A* mutants ($G11A/G11A; nSyb-Gal4 > UAS-EXOSC3$) on days 7 and 14 compared to *Rrp40* controls (WT/WT and $nSyb-Gal4/UAS-EXOSC3$). Data are shown as the mean \pm SEM (ns $p > 0.05$, $*p < 0.05$, and $****p < 0.0001$; unpaired two-tailed t test vs. WT).

(D) Short-term aversive taste memory assay in newly eclosed (day 1, left) and aged (day 14, right) flies. *Rrp40* control (WT/WT) and mutant (*G11A/G11A* or *G146C/G146C*) flies ($n = 10$ per genotype) were food deprived for 24 h prior to testing. A memory assay was performed as described in the STAR Methods. Proboscis extension rates (PERs) are presented as the mean \pm SEM (two-way ANOVA; $*p < 0.05$, $**p < 0.01$, and $***p < 0.001$).

(E) Pan-neuronal expression of human *EXOSC3* ($nSyb-Gal4 > UAS-EXOSC3$) rescues memory deficits in *G11A/G11A* mutants ($G11A/G11A; nSyb-Gal4 > UAS-EXOSC3$) on day 14 compared to controls (WT/WT and $nSyb-Gal4/UAS-EXOSC3$). Flies ($n = 10$ per genotype) were food deprived for 24 h prior to testing. A memory assay was performed as described in the STAR Methods. Proboscis extension rates (PERs) are presented as the mean \pm SEM (two-way ANOVA; $*p < 0.05$, $**p < 0.01$, and $***p < 0.001$).

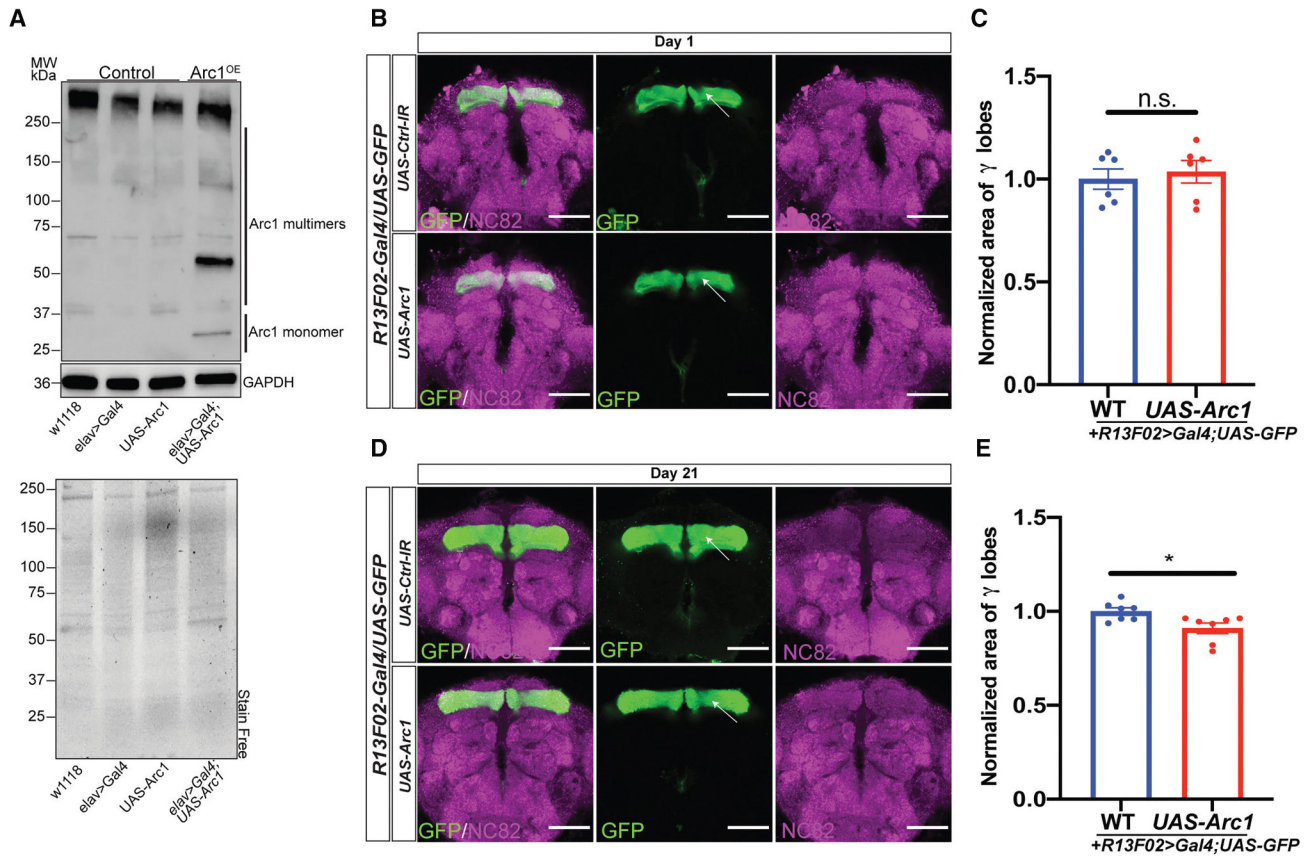


Figure 7. Overexpression of *Arc1* in aged flies induces mushroom body defects

(A) Western blot of head lysates prepared from control flies (*w¹¹¹⁸*, *elav>Gal4*, UAS-*Arc1*) and *Arc1*-overexpressing flies (*elav>Gal4>UAS>Arc1*). Lysates were resolved by SDS-PAGE and probed with antibodies detecting *Arc1* monomeric and multimeric species. GAPDH and stain-free imaging of total protein were used as loading controls.

(B) Confocal images of *Arc1*-overexpressing flies (*UAS-Arc1*, BDSC #37532) and control flies (*R13F02>Gal4/UAS/GFP*; *Control-IR*; *yv; attP40*, BDSC #36303) expressing GFP in mushroom-body γ -lobe neurons via the *R13F02-Gal4* driver (*R13F02-Gal4>UAS-GFP*) collected on day 1. The brains were labeled with anti-GFP (γ -lobe neurons) and anti-NC82 (central complex; magenta). Columns: merged GFP/NC82 (left), GFP alone (middle), and NC82 alone (right). Scale bars, 50 μ m.

(C) Quantification of γ -lobe size from GFP labeling in day 1 control and *Arc1*-overexpressing brains shown in (B). Values represent the mean \pm SD. * $p < 0.05$, ** $p < 0.01$, *** $p < 0.001$, **** $p < 0.0001$, and ns, not significant.

(D) Confocal images of *Arc1*-overexpressing flies (*UAS-Arc1*, BDSC #37532) and control flies (*R13F02>GFP/Control-IR*) (*Control-IR*: BDSC #36303) expressing GFP in mushroom-body γ -lobe neurons via *R13F02-Gal4* on day 21. The brains were labeled with anti-GFP (green) and anti-NC82 (magenta). Columns: merged GFP/NC82 (left), GFP alone (middle), and NC82 alone (right). Scale bars, 50 μ m.

(E) Quantification of γ -lobe size from GFP labeling in day 21 control and *Arc1*-overexpressing brains, shown in (D). Values represent the mean \pm SD. * $p < 0.05$, ** $p < 0.01$, *** $p < 0.001$, **** $p < 0.0001$, and ns, not significant.

KEY RESOURCES TABLE

REAGENT or RESOURCE	SOURCE	IDENTIFIER
Antibodies		
Rabbit anti-Rrp40	Pacific Immunology	N/A
Rabbit anti-Arc1	73	N/A
Mouse anti-GAPDH	ProteinTech	Cat# 60004-1-Ig; RRID: AB_2107436
Mouse 4F3 anti-discs large	Developmental Studies Hybridoma Bank	RRID: AB_528203
Mouse 1D4 anti-Fasciclin II	Developmental Studies Hybridoma Bank (Goodman, C.)	N/A
Mouse anti-nc82	Developmental Studies Hybridoma Bank (Buchner, E.)	N/A
Rabbit anti-GFP	Cell Signaling	Cat# 2956S
Goat anti-Rabbit IgG (H + L) Highly Cross-Adsorbed Secondary Antibody, Alexa Fluor™ 647	Thermo Fisher Scientific	Cat# A-21245; RRID: AB_2535813
Goat anti-Rabbit IgG (H + L) Highly Cross-Adsorbed Secondary Antibody, Alexa Fluor™ 488	Thermo Fisher Scientific	Cat# A-11034; RRID: AB_2576217
Goat anti-Mouse IgG (H + L) Highly Cross-Adsorbed Secondary Antibody, Alexa Fluor™ 647	Thermo Fisher Scientific	Cat# A-21236; RRID: AB_2535805
Goat anti-Mouse IgG (H + L) Highly Cross-Adsorbed Secondary Antibody, Alexa Fluor™ 488	Thermo Fisher Scientific	Cat# A-11029; RRID: AB_2534088
Goat Anti-Mouse IgG (H + L)-HRP Conjugate	Bio-Rad	Cat# #1706516
Goat anti-Rabbit IgG (H + L) Secondary Antibody, HRP	Invitrogen	Cat# 31466
Bacterial and virus strains		
NEB® Turbo Competent E. coli (High Efficiency)	New England Biolabs	Cat# C2984H
DH5α Competent Cells	Thermo Scientific	Cat# EC0112
Chemicals, peptides, and recombinant proteins		
UltraPure™ 1M Tris-HCl, pH 8.0	Thermo Fisher Scientific	Cat# 15568025
KCl (2 M), RNase-free	Thermo Fisher Scientific	Cat# AM9640G
MgCl ₂ (1 M)	Thermo Fisher Scientific	Cat# AM9530G
Triton™ X-100	Millipore Sigma	Cat# T9284-100ML
RNasin® Plus Ribonuclease Inhibitor	Promega	Cat# N2611
Protease Inhibitor Cocktail, 50X	Promega	Cat#G6521
DL-Dithiothreitol solution	Millipore Sigma	Cat# 43816-10ML
Albumin, Bovine Serum, Fraction V, Fatty Acid-Free, Nuclease- and Protease-Free	EMD Millipore	Cat# 126609-5GM
Debris Removal Solution	Miltenyi Biotec	Cat# 30-109-398
32% Paraformaldehyde (formaldehyde) aqueous solution, (1) 100 mL bottle	Electron Microscopy Sciences	Cat#15714-S
Corning® 10X PBS, pH 7.4	VWR	Cat# 45001-130
Tween® 20	Millipore Sigma	Cat# P9416-100ML
SSC Buffer, 20X Solution, 1 L	Research Products International	Cat# S24022-1000.0
ProLong™ Gold Antifade Mountant	Thermo Fisher Scientific	Cat# P36934
Trizol™ Reagent	Thermo Scientific	Cat# 15596026

REAGENT or RESOURCE	SOURCE	IDENTIFIER
E. coli Poly(A) Polymerase	New England Biolabs	Cat# #M0276S
Sucrose ACS 500g	EMD Millipore	Cat# SX1075-1
Caffeine Powder	Sigma Aldrich	Cat# CO750-500G
4-20% Mini-PROTEAN® TGX Stain-Free™ Protein Gels, 12 well, 20 µL #4568095	Bio-Rad	Cat# 456-8095
Everyblot Blocking Buffer	Bio-Rad	Cat# 12010020
Clarity™ Western ECL Substrate	Bio-Rad	Cat# 1705060
ExpressHyb Hybridization Solution	Takara Bio	Cat# 636833
10% Mini-PROTEAN	Bio-Rad	Cat# 4566033
Hybond-N+ membrane	Cytiva	Cat# RPN119B
Licor IRDye 800CW DBCO Infrared Dye, 0.5 mg	LICORbio	Cat# 929-50000
Licor IRDye 680RD DBCO Infrared Dye, 0.5 mg	LICORbio	Cat# 929-50005
Invitrogen ambion SDS, 20% Solution	Thermo Scientific	Cat# AM9820
Critical commercial assays		
Chromium Next GEM Single Cell 3' GEM, Library & Gel Bead Kit v3.1	10X Genomics	PN-1000213
Qubit™ RNA BR Assay Kit	Thermo Fisher Scientific	Q33216
HCR™ Probe (v3.0) Organism: Fruit Fly Target: Arc1 CDS	Molecular Instruments	N/A
HCR™ IF Kit 2° Antibody Probe Donkey Anti-Mouse	Molecular Instruments	N/A
Methyl Alcohol, Anhydrous	Avantor	Cat# 3041-10
PCR-cDNA barcoding kit	Oxford Nanopore Technologies	Cat# SQK-PCB114.24
Trans-Blot Turbo RTA Mini 0.2 µm Nitrocellulose Transfer Kit, for 40 blots	Bio-Rad	Cat# #1704270
Deposited data		
FASTQ reads for single-nucleus RNA-seq of <i>Drosophila</i> fly heads	This study	GSE280166
FASTQ reads for Nanopore PCR-cDNA sequencing of <i>Drosophila</i> fly heads	This study	PRJNA1179429
Raw and processed mass spectrometry data	This study	MSV000099840; PXD070589
Experimental models: Organisms/strains		
<i>D. melanogaster</i> : R13F02-Gal4	BDSC	RRID: BDSC_68383
<i>D. melanogaster</i> : elav-Gal4	BDSC	RRID: BDSC_458
<i>D. melanogaster</i> : nSyb-Gal4	BDSC	RRID: BDSC_51635
<i>D. melanogaster</i> : UAS-Arc1.WT	BDSC	RRID: BDSC_37532
<i>D. melanogaster</i> : UAS-EXOSC3.WT	Morton et al. ³⁹	N/A
<i>D. melanogaster</i> : attP40 (control TRiP RNAi)	BDSC	RRID: BDSC_36304
<i>D. melanogaster</i> : 40XUAS-IVS-mCD8:GFP	BDSC	RRID: BDSC_32195
<i>D. melanogaster</i> : UAS-Rrp40 ^{RNAi}	BDSC	RRID: BDSC_62834
<i>D. melanogaster</i> : UAS-Arc1 ^{RNAi}	BDSC	RRID: BDSC_25954
<i>D. melanogaster</i> : Arc ^{Jesm113}	BDSC	RRID: BDSC_37531
<i>D. melanogaster</i> : Rrp40-G11A/G11A	Bestgene Inc.	N/A
<i>D. melanogaster</i> : Rrp40-G146C/G146C	Bestgene Inc.	N/A
<i>D. melanogaster</i> : Rrp40-WT/WT	Bestgene Inc.	N/A

REAGENT or RESOURCE	SOURCE	IDENTIFIER
Oligonucleotides		
Primer: <i>Rrp40</i> upstream -Forward: GGC AGT GTT GGA AAG TCC T	This study	N/A
Primer: <i>Rrp40</i> upstream -Reverse: GAA GAA GAA TCC ATC GGT GAG G		
Primer: <i>Rrp40</i> downstream -Forward: TTT ACG CGA GAG TCC TGA ATG		
Primer: <i>Rrp40</i> downstream -Reverse: CTT CCA TCT GCT CAT CTC TGA TAG		
5.8s rRNA northern blot probe: 5' CAGCATGGACTGCGATAT GCGTTCAAAATGT/iAzideN/C 3'	Gerstberger et al. ⁵¹	N/A
HCR RNA-FISH DNA probe: Arc1	Molecular Instruments	N/A
Recombinant DNA		
pCFD3-dU6:3gRNA	addgene	Cat# 49410
Software and algorithms		
ImageJ	ImageJ	https://ImageJ.net/ImageJ/ ; RRID: SCR_003070
Imaris	Oxford Instruments	https://imaris.oxinst.com/ ; RRID:SCR_007370
Cell ranger version 7.1.0	10X Genomics	RRID: SCR_017344
Prism 10	GraphPad	https://www.graphpad.com/ ; RRID: SCR_002798
Seurat version v4.2.1	Hao et al. ⁷⁴ ; Butler et al. ⁷⁵ ; Stuart et al. ⁷⁶	RRID:SCR_016341
Loupe Browser v8	10x Genomics	RRID:SCR_018555
MinKNOW	Oxford Nanopore Technologies	RRID:SCR_023196
Minimap 2	Li et al. ⁷⁷	https://github.com/lh3/minimap2/ ; RRID:SCR_018550
Integrative Genomics Viewer	Robinson et al. ⁷⁸	http://www.broadinstitute.org/igv/ ; RRID:SCR_011793